

HST survey of the Orion Nebula Cluster in the H₂O 1.4 μm absorption band: III. The population of sub-stellar binary companions

GIOVANNI MARIA STRAMPELLI,^{1,2,3} JONATHAN AGUILAR,¹ LAURENT PUEYO,² ANTONIO APARICIO,^{3,4} MARIO GENNARO,²
LEONARDO UBEDA,² AND MASSIMO ROBERTO^{5,2}

¹*Johns Hopkins University, 3400 N. Charles Street, Baltimore, MD 21218, USA*

²*Space Telescope Science Institute, 3700 San Martin Dr, Baltimore, MD 21218, USA*

³*Department of Astrophysics, University of La Laguna, Av. Astrofísico Francisco Sánchez, 38200 San Cristbal de La Laguna, Tenerife, Canary Islands, Spain*

⁴*Instituto de Astrofísica de Canarias, C. Va Lctea, 38200, San Cristbal de La Laguna, Tenerife, Canary Islands, Spain*

⁵*Johns Hopkins University 3400 N. Charles Street Baltimore, MD 21218, USA*

(Received November 16, 2019; Accepted April 30, 2020)

Submitted to ApJ

ABSTRACT

We present new results concerning the sub-stellar binary population in the Orion Nebula Cluster (ONC). Using the Karhunen-Loève Image Projection (KLIP) algorithm, we have reprocessed images taken with the IR channel of the Wide Field Camera 3 mounted on the *Hubble Space Telescope* to unveil faint close companions in the wings of the stellar PSFs. Starting with a sample of 1392 bona-fide not saturated cluster members, we detect 39 close-pairs cluster candidates with separation $0.16'' - 0.77''$. The primary masses span a range $M_p \sim 0.015 - 1.27 M_\odot$ whereas for the companions we derive $M_c \sim 0.004 - 0.54 M_\odot$. Of these 39 binary systems, 18 were already known while the remaining 21 are new detections. Correcting for completeness and combining our catalog with previously detected ONC binaries, we obtain an overall binary fraction of $11.5\% \pm 0.9\%$. Compared to other star forming regions, our multiplicity function is ~ 2 smaller than e.g. Taurus, while compared to the binaries in the field we obtain comparable values. We analyze the mass function of the binaries, finding differences between the mass distribution of binaries and single stars and between primary and companion mass distributions. The mass ratio shows a bottom-heavy distribution with median value of $M_c/M_p \sim 0.25$. Overall our results suggest that ONC binaries may represent a template for the typical population of field binaries, supporting the hypothesis that the ONC may be regarded as a most typical star forming region in the Milky Way.

Keywords: binaries — stars: pre-main sequence — stars: low-mass — open clusters and associations: individual (Orion Nebula Cluster)

1. INTRODUCTION

Binary stars are coeval pairs of stars born in the same environment, with the same metallicity, but with different mass. Understanding their properties provide us with key information on stellar evolution, from the early phases of star formation to the most violent phenomenology that may characterize the final moments of their life. In what concern young systems, knowing the

effective temperature and absolute luminosity of a pair can constrain theoretical models developed to predict isochrones and evolutionary tracks on the HR diagrams during the Pre-Main Sequence phase (Gennaro et al. 2012; Stassun et al. 2014). Ignoring the presence of binaries, on the other hand, represents a nuisance that may affect the statistical analysis of the same HR diagrams (Jerabkova et al. 2019).

The distribution and frequency of binary systems with a substellar companions has been the object of several studies (see e.g. Duchêne & Kraus 2013, review and reference therein). In principle, very low-mass compan-

ions (down to the deuterium burning limit, Spiegel et al. 2011) might form like stars through early fragmentation and gravitational collapse of a common pre-stellar core, or like planets in a circumstellar disk, reaching their observed wide orbits through migration or scattering. Characterizing the population of low-mass companion can thus shed light on the mechanism of star and planet formation at the lower and upper boundary, respectively, of their mass range.

Since substellar objects are unable to sustain hydrogen fusion in their cores and quickly fade away becoming undetectable, young stellar clusters in the solar vicinity are ideal for large statistical studies. Using direct imaging techniques, the main observational challenge is that objects potentially resolved may be hidden under the extended Point Spread Function (PSF) wings of the primary. No-detections only provide upper limits on the companion frequency within a wide range of mass and semi-major axis (SMA). To probe beyond these limits, image processing techniques that remove the PSF while preserving the flux of the companion have been developed.

The key element in performing PSF subtraction is having an accurate template for the PSF itself. In 1-to-1 PSF subtraction, also called Reference Differential Imaging, a single reference PSF is directly subtracted from the science image. For the two PSFs to match, reference and target images should be acquired maintaining the same instrument configuration, in the same part of the sky, and as close in time as possible. This helps reducing changes in the PSF due to variations resulting from e.g. the unstable thermal environment in a low-earth orbit environment, or instrument flexures and variable atmospheric conditions on the ground. In practice, if only one reference PSF is available, the results of the subtraction will always be subject to a variety of systematic and random differences between the reference and science images. To reduce the impact of using a particular realization of the reference PSF on the subtraction residuals, it is advantageous to combine multiple PSFs. A variety of observing strategies and algorithms have been developed in order to optimally combine multiple reference PSF images (e.g. Marois et al. 2014). Eventually, in the case of a positive detection, finding a faint object in the immediate vicinity of a star does not provide conclusive evidence of a physical association. Complementary information, such as common proper or parallactic motion, is needed to disentangle real pairs from random alignments. Lacking multiple epoch data, the presence of photospheric features characteristics of young low mass objects may provide strong indication for real binary systems.

In this paper we presents the results of a search for substellar companions in the Orion Nebula Cluster (ONC) based on data obtained with the Hubble Space Telescope (HST). The ONC is ideal for this type of investigation: it is massive enough ($\sim 2000M_{\odot}$) to provide us with a rich sample of targets and sufficiently nearby ($\simeq 400$ pc; Kuhn et al. 2019) that the the angular scale of a WFC3/IR pixel, $0.13''$, corresponds to a physical separation of $\simeq 50$ AU, i.e. the distance of Pluto to the Sun at aphelion.

Our strategy is based on reprocessing standard wide-field imaging data with advanced PSF subtraction techniques, namely the KLIP algorithm Soummer et al. (2012), fully exploiting the exquisite stability of the HST. In particular, we have used a dataset consisting of images obtained with the IR channel of the Wide Field Camera 3 (*HST*/WFC3) through a pair of filters tailored to measure the depth of the $1.4\ \mu\text{m}$ H₂O absorption feature: F139M (in band) and F130N (adjacent, line-free continuum). In the first paper of this series (Robberto et al., 2020, ApJ submitted, hereafter Paper I with corresponding catalog of sources: Catalog I) we have shown that the presence of the water absorption feature in the atmosphere of low luminosity sources can be used to separate the substellar cluster population of the Orion Nebula Cluster (ONC) from background stars and galaxies. The flux decrease in the F139M filter relative to the nearby F130N continuum produces a negative (blue) $m_{130}-m_{139}$ color index highly sensitive to the effective temperature down to $T_{\text{eff}} \simeq 2800$ K ($\sim 0.06 M_{\odot}$); below this value the absorption feature remains strong but with a weaker dependence on the effective temperature, reaching $m_{130}-m_{139} \simeq -0.5$ at temperature $T_{\text{eff}} \simeq 2200$ K ($\sim 0.01 M_{\odot}$).

The possibility of discriminating low-mass objects from the population of reddened field stars has allowed Gennaro & Robberto (2020, ApJ submitted, hereafter Paper II) to investigate the shape of the initial mass function of “field” cluster members down to planetary masses. Catalog I, however, only reaches separations as small as $0.8''$ (320 AU), inside of which the search for binary candidates is hampered by PSF blending. By applying the KLIP algorithm and advanced statistical analysis to discard false positive detections, we are able to provide a new, comprehensive picture of binarity in the ONC from 70 to 310 AU

In Section 2, we summarize the main characteristics of the dataset. In Section 3 we present our methodology whereas in Section 4 we present the result of our search. We discuss the main properties of our sample in Section 5, while in Section 6 we summarize our findings.

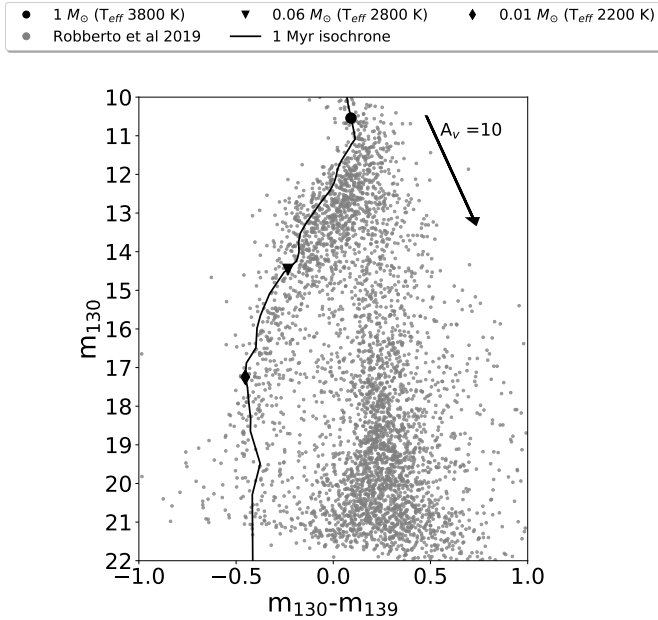


Figure 1. Color magnitude diagram in filters F130N, F139M for all sources detected in the ONC field. The black line is a 1 Myr isochrone with three characteristic masses, from bottom to top $M_{\odot} = 0.02, 0.08$ and 1.

2. DATASET

The Cycle 22 *HST* Treasury Program “The Orion Nebula Cluster as a Paradigm of Star Formation” (GO-13826, P.I. M. Robberto) aims at reconstructing the low-mass IMF down to $\sim 5M_{Jup}$ in the ONC. Paper I presents the survey strategy, sensitivity limits and completeness analysis, leading to a census of the stellar and substellar population in the ONC down to few Jupiter masses in the F130N and F139M filters. The 208 images taken in each filter produce wide field mosaics covering an area of $\sim 1/6$ of a square degree. The number of *unique* sources, either ONC members or background stars and galaxies, is 4504 but in this paper we reprocess the full dataset of more than ~ 8700 source detections, as the mosaicing strategy allowed detecting the same sources during multiple visits. Figure 1 shows the color-magnitude diagram for all 4504 sources, with the clear separation between the cluster population at the top and left side of the diagram, and the background sources at bottom right, with positive $m_{130} - m_{139}$ color. A 1 Myr isochrone, adapted from the BT-Settl model to correct for the discrepancy between the model and the data, is overplotted in red color up to a mass $M \lesssim 0.75M_{\odot}$ (see Paper I for a description of the models and of their semi-empirical calibration). For masses $\geq 0.75M_{\odot}$ we departed from the BT-Settl model, adopting instead the MESA isochrones and Stellar Tracks (MIST) for the

WFC3 IR channel in our F130N and F139M filters (Dotter 2016; Choi et al. 2016).

3. DATA ANALYSIS

3.1. Catalogs of reference and target stars

As reported in Paper I, saturation in the F130N filter starts at $m \simeq 10.9$ while the noise floor is at $m \simeq 22$, setting the magnitude limits of the primaries and companions we are able to analyze.

Our input catalog of targets contained 8210 individual detections (of which 4220 unique) with m_{130} magnitudes in the range 10.9 to 22, about 50% of them corresponding to repeated detections of the same sources.

Our PSF subtraction technique requires a reference catalog of sources uncontaminated by astrophysical or instrumental noise. We create it from our sample, perform several clean-up steps:

1. *Visual binaries removal:* We remove from our catalog 157 unique pairs, for a total of 623 total entries with a neighbor closer than $1.5''$ projected distance according to the Catalog I. In this way we avoid contamination from nearby neighbours whose PSFs wings may affect the region searched for low-mass companions.
2. *Bad pixel removal:* The dataset of full-frame WFC3 images is cleaned from cosmic-rays event in the early stages of standard data processing thanks to the non-destructive sampling of the accumulating signal. Static bad pixels are also flagged by the pipeline. However, we perform an independent check by stacking the images and applying a 10σ threshold to the distribution of median pixel values. We didn’t find any detection with a flagged pixel closer than $\sim 0.8''$ in any visit.
3. *ACS catalog matching:* *HST*/ACS survey of Robberto et al. (2013) provides a high-resolution morphological classification of the sources in the ONC. By cross-matching the ACS catalog with our list of WFC3 detections, we discard all objects flagged as non-stellar, i.e. silhouette disk, proplyds, sources with evidence of jets/photoionization, Herbig-Haro objects, resolved galaxies. We discarded a total of 222 unique objects for a total of 458 entries from the catalog

Applying these selection criteria we end up with with a catalog of 7129 individual sources, counting multiple observations of the same object separately.

The next step is to create “postage stamps” centered on each source and perform the PSF subtraction inside

this area. In setting our 11×11 ($1.5'' \times 1.5''$) pixel stamp size we consider the following factors:

- the area must be large enough to contain the bright wings of the PSF, for sources matching our assumed range of magnitudes;
- the area must have enough pixels to provide a meaningful noise calculation. Detections of close companions are affected by small number statistics and a correction to the estimated contrast and SNR has to be applied (Mawet et al. 2014). The following argument shows that the correction is very small for an 11×11 stamp. The number of λ/D resolution elements per pixel for WFC3 in the F139M filter is close to 1, i.e. WFC3-IR is significantly undersampled. Therefore, a 11 pixel stamp contains about the same number of resolution elements. The correction factor to the SNR is given by $(\sqrt{1 + 1/n})^{-1}$, which for $n = 121$ is 0.996. Therefore, the sample size does not represent a significant source of uncertainty vs. other noise sources, e.g. photon or read noise.
- the area must be small enough so that tiles do not overlap; having rejected from our catalog objects with a nearest companion closer than $1.5''$, this results in a tile half-size of $0.7''$. With a WFC3 pixel scale of $0.13'' \text{ pixel}^{-1}$, the tile half-size translates to a radius of approximately 280 AU distance from a point source in the ONC.

3.2. PSF subtraction

Accurate PSF subtraction depends strongly on the quality of the reference PSF, a task greatly simplified by the stability of the Hubble Space Telescope which has enabled the compilation of libraries of PSF models for reference differential imaging (e.g. Choquet et al. 2014). Still, for the most accurate PSF subtraction one has to deal with the field distortion of WFC3 and the small but not negligible time-dependence of the HST focus. These effects make the PSF both spatially and time dependent. Our strategy is especially well-suited for handling both effects.

It consists in dividing the field of view into 100 equal cells, each cell small enough to neglect local PSF distortion but large enough to build a local PSF library containing enough stars to build an accurate model.

For each cell, PSF subtraction is then performed as follows:

- the postage stamp for all stars in the cell are stacked together into a single data cube;

- iterating through the data cube, each stamp is assumed as the science image;
- a reference model of the PSF for subtraction is constructed selecting from the remaining postage stamps those with a photometric error $\sigma_{F130N} \leq 0.01$;
- the PSF of the target star was in then removed using the Karhunen-Loève Image Projection (KLIP) algorithm (Soummer et al. 2012).

For each target, we chose the number of modes which simultaneously minimize the standard deviation of the residual image while maximizing the counts of the brightest residual pixel.

To build a preliminary catalog of candidate binaries, we analyze the position of the brightest pixel of the residual images of each target. To be labeled as a candidate detection, at this early stage, we require that:

- the pixels with the highest flux in each residual must be within one pixel in both filters and in all available visits when the source is observed with different telescope orientations;
- to candidate must be detected in at least two different KLIP modes.

The one pixel distance (rather than zero) is needed to take into account possible misalignments of the center of the stars in the reference library, due to the under-sampled PSF and lack of dithering in the survey. This reflects in an accuracy of our separation estimates of about $1/2$ pixel, i.e. $0.07''$ or 28 AU at the distance of the ONC.

3.3. Cluster and Background candidates

The inspection of the residuals immediately after PSF subtraction reveals a large number of candidate companions, but further down-selection has to be applied to reject sources that presumably do not belong to the ONC. To separate cluster stars from background sources we use the position of the stars on the CMD. As shown in Paper I, the pair of filters chosen for this survey is sensitive to the depth of the $1.4 \mu\text{m}$ H_2O absorption band. This temperature-sensitive feature is prominent in the atmosphere of M-type stars and brown dwarfs, down to planetary-mass objects and can be than used to separate the substellar cluster population of the ONC from background stars and galaxies. Following Paper I we consider a source to be a ONC member if it lies in the area delimited by the 1 Myr isochrone introduced in Section 2, reddened by $A_V = 10$ mag. Any companion candidates bluer (redder) than this isochrone is labeled as cluster (background). In Paper I we found good

agreement between this simple approach and a more rigorous Bayesian statistical treatment. At the end of this process we obtained 2797 multiple visits cluster sources, with 1392 *unique* targets for our KLIP PSF subtraction algorithm.

3.4. Companion Photometry

Since the WFC3/IR PSF is highly undersampled, after PSF subtraction we expect most of the flux from a faint candidate companion to be contained within a few pixels. Thus, to derive the total flux one has to apply a large and rather uncertain aperture correction. To evaluate it, we analyze a sample of isolated bright stars in our catalog comparing their flux around the brightest pixels with their total flux. This analysis shows that about 1/3 of the flux is contained within the brightest pixel and $\sim 60\%$ within the four adjacent brightest pixels. The distribution of relative fluxes for the four brightest pixels is narrower than the distribution for the single pixel. Therefore, we perform our photometry of the companions using a 4-pixel aperture, deriving the aperture correction to the total flux through comparison with the Catalog I PSF photometry. Specifically, for each isolated source in Catalog I we built a square 2x2 pixel mask placed so that one pixel always coincides with the brightest pixel of the original image. After probing the 4 possible mask positions, we record the maximum value of the total counts as c_{4p} . The magnitude for each primary is then calculated as:

$$m_{4p} = -2.5 \log_{10}(c_{4p}) + C \quad (1)$$

where C is a normalization factor between the 4-pixel photometry and PSF photometry ($C_{m_{130}} = 21.35 \pm 0.049$, $C_{m_{130}-m_{139}} = -0.002 \pm 0.031$). We then determine C as the mean of the difference between the PSF photometry and the 4-pixel photometry of each primary:

$$\langle m_{PSF} - m_{4p} \rangle = C \quad (2)$$

Measuring c_{4p} for each detected companion and using equations 1 and the value of C from equation 2, we determine the magnitudes of our candidate companions. Our estimate of the total uncertainty takes into account the uncertainty on the counts of the candidate, on the background counts in the 4-pixel aperture, and on the estimated conversion factor between the PSF and the 4-pixel system (the standard deviation of the sample we used to evaluate the conversion factor).

Having determined the photometry for each candidate, a new selection is applied keeping all the cluster pairs with companion magnitude in the range $10.9 \geq \text{mag}_{130} \geq 22$ (following a similar approach as the one

mentioned in Section 3.3) and with absolute value of the $m_{130}-m_{139}$ color ≤ 1 to reject noisy outliers. This results in a preliminary selection of 145 cluster candidate binaries.

3.5. Real vs. false positive detections

To assess our ability to separate plausible candidate from instrument induced false positive detections, we perform an extensive set of simulations to determine the Receiving Operating Characteristic (ROC) curves (see Appendix A for an explanation of ROC curve construction) for each binary configuration in our preliminary catalog. A configuration is specified by three parameters a) brightness of the primary, b) contrast between primary and companion, and c) separation and KLIP mode used during the PSF subtraction phase. We use the ROC curves to derive three other quantities we can use to make the following selections on our candidates:

- the Area Under the Curve (AUC) of the ROC: the AUC provides us with a good indication of how well the distribution of the true positive rate (TPR, i.e. detection of companions injected in our simulations) is separated from the distribution of the false positive rate (FPR, i.e. detection of noise peaks that may have been erroneously determined to be companions). A AUC curve of 0.5 indicates that there is no possibility of separating the two distributions, whereas an AUC=1 represents perfect separation. An analysis of the results provided by the simulations led us to select a candidates only when the corresponding configuration provides an AUC ≥ 0.7 .
- false positive probability and SNR threshold: as explained in Appendix A, for each given configuration, the ROC curve is built sliding a SNR threshold across the TPR and FPR distributions. We can therefore invert this process: given the ROC curve for the certain configuration and having determined a limit to the probability for a detection to be a false positive, we find the corresponding SNR that we can use as a threshold for the detection. Because each candidate is found using multiple independent detections (different filters and possibly different locations on the detector for each visit), we multiply the false positive probabilities of each detection (FP') to obtain an overall false positive probability for the whole candidate (FP). In particular, if we assume FP' to be the same for each detection, it is:

$$FP = FP'^{(N_f \times N_v)} \quad (3)$$

where N_f is the number of filters and N_v is the number of visit for the candidate. Inverting this relation we find FP' as a function of FP . Having set FP' , we can find the corresponding SNR threshold from the ROC. With 1392 primaries to be searched, assuming an overall false positive probability $FP = 0.2\%$ for each candidate, we expect ~ 3 false positive detection in our final catalog of binaries. We have verified that this probability value represents an optimal trade-off. A further reduction, i.e. a more aggressive reduction of false positives, would imply higher detection thresholds that would lead to reject strong previously known true detections. Viceversa, relaxing the threshold would cause a large increase in the number of false positives beyond the acceptable rate of 50-100 smaller than the expected detection signal (as a point of reference the expected binary fraction is 10-20 percent as per Kraus and Duchene)

- ratio of true positives over false positives (R): for each candidate detection we binned the TPR and FPR distributions in bins of 0.5 SNR and we evaluate the ratio of true positive over false positive in the same bin corresponding to the candidate SNR detection. This parameter give us an indication about how common the candidate SNR is in the distribution of false positive and true positive. Because each candidate results from multiple detections, we keep only candidates with with an $R_{median} \geq 3$.

As a by-product of our simulations, we also obtain the amount of flux lost due to over-subtraction (see Pueyo 2016 and reference therein), deriving the correction to apply to the photometry of our candidate companions, with the relative errors. Moreover, from the distributions of TPR and FPR we can also evaluate the contrast curves as a function of the magnitude of the primary, contrast and separation. Averaging all data we obtain the contrast curves shown in Fig. 2.

The preceding analysis is not designed to distinguish between true companions and other astrophysical sources of false positives. These include residual contamination from nearby stars and light emitted by circumstellar material. Detector persistence may cause "ghosts" of very bright stars into the subsequent exposures, but they also appear as extended structures that can be easily identified and generally decay within one visit (see Paper I). This is why to conclude this candidate selection we visually inspect all our selected candidates looking for extended residuals.

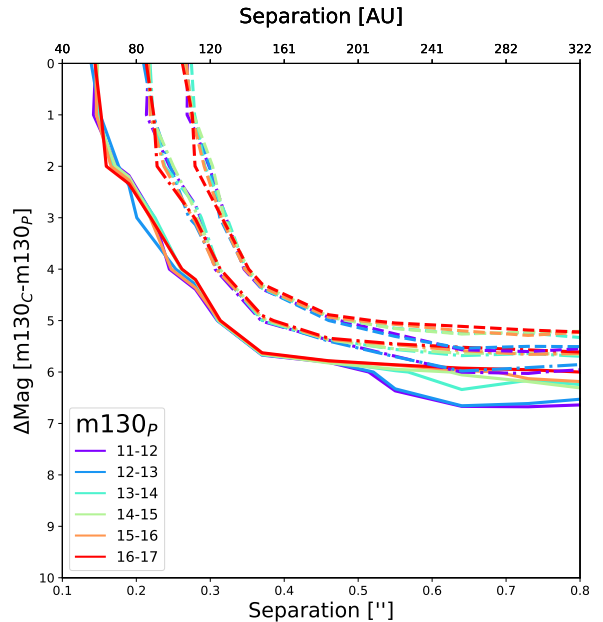


Figure 2. Averaged contrast curve over different visits and KLIP modes for each magnitude bin of the primary star and delta magnitude between companion and primary and projected separation. the three families of curves correspond to completeness $C = 0.1, 0.3, 0.5$

3.6. Companion Mass Determination

To estimate the mass of our substellar companions we start with an analysis of the primaries and isolated ONC stars. Figure 3 shows the comparison between the masses estimated by Da Rio et al. (2012) using the Baraffe et al. (1998) evolutionary models ($DR2012_{mass}$) and the masses obtained from our de-reddened WFC3 photometry and the 1 Myr isochrone ($WFC3_{mass}$, grey points). We use the value of A_V determined by Da Rio et al. when available, otherwise we use the A_V estimate from Paper I, with negative A_V values are set to $A_V = 0$. In the range of $WFC3_{mass}$ between $0.075 - 1.5 M_\odot$ (vertical lines in the plot) we observe good correlation with some systematic difference between the two mass estimates. Below this range, the scatter increases, an indication of the difficulty of DR2012 optical survey in dealing with the reddest and faintest sources of their sample. To reconcile the two datasets, we use an empirical isochrone, fitting the relation between the $DR2012_{mass}$ and the $WFC3_{mass}$ in the $0.075 - 1.5 M_\odot$ mass range with a spline function as follow:

- we bin the distribution of $F130N_{mass}$ between $0.075 - 1.5 M_\odot$. To have bins perpendicular to the $DR2012_{mass} = WFC3_{mass}$ relation (blue line in

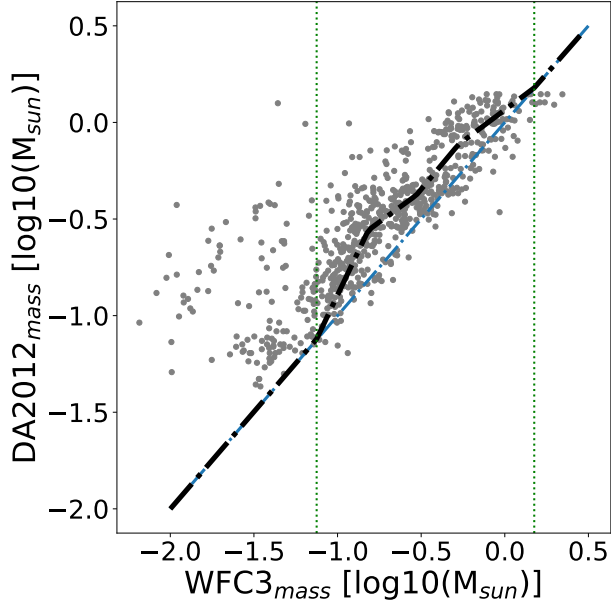


Figure 3. Da Rio et al. DR2012 vs. WFC3 masses (grey points). The two green dotted lines mark the value for $WFC3_{mass} = 0.075 M_{\odot}$ and $1.5 M_{\odot}$. The blue dotted line shows the locus of point where $DR2012_{mass} = WFC3_{mass}$, while the black dotted line shows the final spline fit of the data.

Figure 3) we apply a rotation matrix to the data by an angle of 45 degree;

- we apply a 3-sigma cut to the distribution of each bin to exclude outliers;
- we rotate back the data and we fit a spline matching the 1 Myr isochone outside the $0.075 - 1.5 M_{\odot}$ $WFC3_{mass}$ range and the median green point otherwise (black dotted line in Figure 3).

In the substellar regime, instead, we only use our WFC3 data relying on the strong correlation between mass and stellar flux (m_{130}), as evidenced by the color-magnitude diagram (Figure 1).

Finally, to evaluate the mass of our candidate binaries, we assign the same A_V values to both components and then evaluate the mass of the companion using the spline curve.

3.7. Completeness limit

The completeness of our survey depends on the mass of the primary, the mass ratio of potential candidate and their separation, i.e. the projected SMA. This function, marginalized over the mass of the primaries, can be represented by a set of completeness curves for the mass

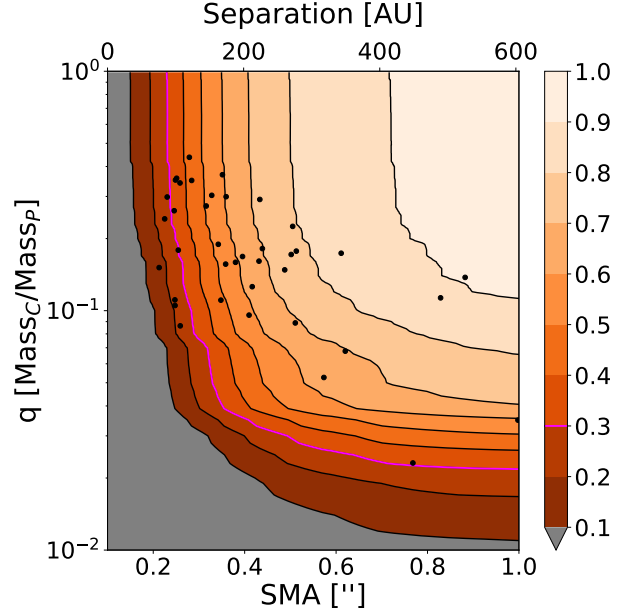


Figure 4. Mass ratio completeness curves estimated as a function SMA with the color coding the value of the completeness. The black dots marks position of each detection on the plot. The magenta line marks the 30% limit below which we only choose candidate with two or more visits.

ratio of the candidate and separation. Completeness as a function of the magnitude of the primary, companion, and visual separations can be obtained by direct inspection of the family of ROC curves discussed in Section 3.5. It can then be converted in a completeness as a function of primary mass, mass ratio and deprojected orbital SMA. This last step is carried out using the following procedure:

- we interpolate over a finer grid both in mass ratio and separation.
- following Brandt et al. (2014), we integrate over all the possible semi-major axes (s) between 0 and 1.8 using a piecewise function $p(s)$:

$$p(s) \simeq \begin{cases} 1.3s & 0 \leq s \leq 1 \\ -\frac{35}{32}(s - \frac{9}{5}) & 1 < s < 1.8 \end{cases} \quad (4)$$

We then use this completeness map to apply a final selection to our catalog of candidates to reject any detection with completeness smaller than 10% or between 10%-30% and with only one visit (i.e. the most likely to be one of the few false positive we expect, since our FP analysis was carried out using single visits). At the

end of this selection process, we obtaining a final catalog of 39 reliable cluster candidates binaries out of 1392 original cluster targets.

Figure 4 shows the final completeness curves as a function of separation in SMA, the black dots mark the position of our detections on the completeness map. The magenta line show the 30% completeness cut we apply to our single visit detection, while the gray area shows the space of parameters in the plot where we always reject candidates because completeness is smaller than 10%.

4. RESULTS

4.1. *Catalog of KLIP-detected candidate cluster binaries*

The analysis described in Section 3 provides us with a total of 39 candidate cluster binaries with separation in the range $1.26 - 5.9$ pixels ($0.16'' - 0.77''$), corresponding to about $66 - 309$ AU projected distance from the primary assuming a distance of 403 pc (Kuhn et al. 2019). The primary masses range between $0.015 M_{\odot} - 1.27 M_{\odot}$

while the companions are in the range $0.004 M_{\odot} - 0.54 M_{\odot}$.

Table 1 shows the physical and photometric properties of the 39 candidates. Column (1) shows the entry number in the catalog; columns (2) and (3) show the Right Ascension and Declination for Equinox J2000.0; columns (4) to (11) list the m_{130} magnitude and the $m_{130} - m_{139}$ color with their relative uncertainties for both primary (P) and companion (C); columns (12) to (15) show the estimated mass from F130N photometry, with its uncertainty, for both primary and companion in units of Solar mass. The last three columns list the position angle, the separation between primary and companion, and the distance of the system from the core of the cluster (identified by the position of θ^1 Ori-C).

In Appendix B we present a gallery of postage stamps (Figure 17-18) showing the co-added images before and after KLIP subtraction for each candidate, the companions generally appearing as bright single pixels in each residual image due to the WFC3/IR sub-sampling. Each postage stamp has dimensions $2'' \times 2''$ and is rotated so that north is up and east to the left.

Table 1. Candidate Binaries catalog (KLIP)

ID	R _{ap}	Dec _p	mag130 _p	color _p	dmag130 _p	dcolor _p	mag130 _c	color _c	dmag130 _c	dcolor _c	mass _p	mass _c	emass _p	emass _c	PA	Sep	SepOrbC
(-)	(deg)	(deg)	(mag)	(mag)	(mag)	(mag)	(mag)	(mag)	(mag)	(mag)	(solMass)	(solMass)	(solMass)	(solMass)	(deg)	(arcsec)	(arcsec)
0	83.65873105	-5.461256454	12.7852	0.07241	0.06655	0.00258	14.79325	-0.1649	0.06521	0.10838	0.265761	0.045624	0.007075	0.001164	11.04	0.39	630.53
1	83.75715053	-5.452742454	13.6095	-0.18075	0.01708	0.0045	15.57923	-0.38044	0.03513	0.06504	0.119621	0.031277	0.000737	0.000623	99.61	0.19	316.95
2	83.77675985	-5.451311859	12.7123	-0.27704	0.01868	0.00997	13.52197	-0.55827	0.05769	0.10461	0.280446	0.100214	0.002345	0.002273	280.28	0.19	268.14
3	83.77159336	-5.434358914	13.4775	-0.07256	0.02798	0.0222	16.49632	-0.79747	0.03127	0.04469	0.151852	0.017179	0.001491	0.000305	354.69	0.64	233.43
4	83.78028406	-5.436474308	15.3643	0.10603	0.01405	0.01473	18.24483	-0.16565	0.03714	0.06303	0.183497	0.020358	0.001036	0.000866	9.79	0.19	217.7
5	83.83343099	-5.486611088	13.4015	0.16228	0.17164	0.02449	14.99455	-0.26626	0.04088	0.05973	0.666812	0.115873	0.075648	0.003052	337.9	0.47	353.03
6	83.84672012	-5.476080805	13.6243	-0.17387	0.001	0.00336	19.94556	-0.54334	0.1797	0.2833	0.132205	0.004614	3.5e-05	0.000223	191.76	0.77	327.13
7	83.89252874	-5.455090951	11.8697	0.02297	0.01133	0.03316	15.77574	-0.51272	0.02497	0.04258	0.519625	0.027329	0.003795	0.000757	134.19	0.44	355.41
8	83.61902968	-5.509038831	14.4798	-0.12672	0.01402	0.0054	20.09559	-0.55557	0.09975	0.28998	0.064618	0.004378	0.000643	0.000124	263.09	0.48	837.1
9	83.82263551	-5.537828912	15.0015	-0.00517	0.00923	0.00788	16.19856	-0.36395	0.0304	0.05199	0.138769	0.048765	0.000325	0.000543	8.86	0.19	533.54
10	83.88307815	-5.52992167	14.6918	-0.21926	0.01524	0.00222	19.26116	-0.3466	0.0438	0.08264	0.047936	0.005304	0.000267	5.2e-05	52.26	0.27	555.71
11	83.95476263	-5.559047659	16.8017	-0.0107	0.01704	0.01693	19.66101	-0.37798	0.04246	0.07579	0.014534	0.005086	0.000129	5e-05	183.71	0.22	782.38
12	83.89670965	-5.448594714	12.1409	0.0594	0.00886	0.01629	14.04119	0.12296	0.03058	0.05044	0.495625	0.088725	0.002556	0.001455	276.57	0.2	352.27
13	83.84242884	-5.443706152	11.295	0.19391	0.00395	0.00074	12.32212	0.30177	0.06507	0.13168	1.237085	0.540864	0.002806	0.030071	283.37	0.21	212.6
14	83.87796088	-5.408648543	12.6713	-0.1118	0.03893	0.02001	14.95313	-0.5236	0.0352	0.05679	0.286316	0.042394	0.004905	0.000628	302.46	0.38	224.4
15	83.82474913	-5.426100713	12.2306	0.04893	0.03399	9e-05	14.11821	-0.0027	0.05342	0.08013	0.406357	0.076947	0.009162	0.003184	348.93	0.26	132.99
16	83.72936023	-5.424836418	12.1775	0.04272	0.00146	0.00087	14.31968	-0.24743	0.04968	0.07978	0.472033	0.073861	0.000417	0.001101	51.6	0.28	345.24
17	83.72843059	-5.420142975	12.872	-0.1633	0.04357	0.00869	14.36475	0.15954	0.05711	0.08939	0.235225	0.064372	0.003889	0.00266	325.05	0.24	342.58
18	83.76287689	-5.37716716	11.7742	-0.00565	0.00886	0.01562	14.66854	0.06643	0.03497	0.05352	0.54935	0.047472	0.002964	0.000624	192.6	0.2	205.54
19	83.8540066	-5.400418165	12.8879	0.2529	0.02858	0.02178	14.59045	-0.08418	0.03732	0.06801	0.888352	0.141468	0.016308	0.003351	255.61	0.29	133.26
20	83.85195641	-5.400290404	13.1041	-0.08161	0.05475	0.01808	14.50296	-0.34182	0.03761	0.06597	0.222372	0.066542	0.004893	0.001752	293.64	0.28	126.07
21	83.82696282	-5.401934612	11.734	0.17088	0.01441	0.00394	16.60982	-0.52286	0.04746	0.08143	0.664391	0.015354	0.006383	0.000452	218.71	0.59	53.45
22	83.82851021	-5.373045614	13.4312	0.09716	0.07249	0.00778	14.3886	-0.3652	0.03982	0.07265	0.386487	0.117198	0.019113	0.002972	321.23	0.25	69.73
23	83.85038408	-5.359054015	12.4144	0.05594	0.16081	0.02832	13.75559	-0.08395	0.03971	0.05803	0.502218	0.112976	0.051514	0.002964	279.68	0.39	158.94
24	83.80338979	-5.345419412	11.3224	0.17154	0.08285	0.03132	13.0126	0.00255	0.03685	0.06362	0.910202	0.146558	0.045441	0.003309	84.52	0.33	168.46
25	83.94418968	-5.373398132	12.3236	-0.01377	0.01082	0.00836	13.83882	0.10386	0.04147	0.06897	0.358728	0.086737	0.002629	0.001984	283.55	0.17	455.97
26	83.9590678	-5.354670298	12.9224	0.0274	0.00393	0.00013	15.56152	-0.21944	0.04992	0.08604	0.279615	0.035214	0.000489	0.000885	263.01	0.32	521.21
27	83.91659751	-5.37407979	14.8903	0.19968	0.00154	0.00207	16.45456	-0.23877	0.04946	0.08087	0.147277	0.043943	5.4e-05	0.000883	276.93	0.18	357.29

NOTE—Table 1 is published in its entirety in the machine-readable format. A portion is shown here for guidance regarding its form and content.

Table 2. Candidate Binaries catalog (Paper I)

ID	R _{ap}	Dec _p	mag130 _p	color _p	dmag130 _p	dcolor _p	mag130 _c	color _c	dmag130 _c	dcolor _c	mass _p	mass _c	emass _p	emass _c	PA	Sep	SepOric
(-)	(deg)	(deg)	(mag)	(mag)	(mag)	(mag)	(mag)	(mag)	(mag)	(mag)	(solMass)	(solMass)	(solMass)	(solMass)	(deg)	(arcsec)	(arcsec)
39	83.67010811	-5.469291606	12.4762	-0.1028	0.0105	0.02419	12.6109	-0.0753	0.17544	0.01007	0.31939	0.294837	0.002017	0.026015	52.49	0.23	606.5
40	83.7861492	-5.483746113	12.5467	0.25674	0.0203	0.00317	13.2935	0.2766	0.03924	0.01055	0.304773	0.148041	0.003707	0.001391	100.11	1.73	358.21
41	83.75904395	-5.486073354	12.2413	0.13568	0.00245	0.00819	12.9594	0.1272	0.03694	0.02989	0.472413	0.288703	0.000702	0.004652	91.1	1.1	407.88
42	83.7648425	-5.490518796	12.4288	0.08384	0.017	0.01154	12.8926	0.20911	0.33596	0.04195	0.392846	0.291612	0.004566	0.051289	161.56	0.57	411.36
43	83.8069495	-5.479491472	12.0332	0.09606	0.23364	0.06372	12.5605	0.10666	0.20579	0.03443	0.746202	0.450407	0.136334	0.060834	70.46	0.37	326.03
44	83.67804089	-5.477043065	11.8368	-0.01121	0.01237	0.0096	12.9269	0.09626	0.70721	0.06328	0.970304	0.420492	0.00626	0.325515	147.16	0.51	595.74
45	83.71943096	-5.495858274	12.1265	0.09143	0.13229	0.01538	12.7255	0.01296	0.01626	0.02557	0.620919	0.373322	0.054193	0.00396	6.01	0.39	523.0
46	83.78686627	-5.530307995	11.5871	0.17012	0.19642	0.0366	11.7648	0.11608	0.67489	0.06516	0.933022	0.847697	0.13524	0.461341	37.83	0.29	518.98
47	83.85699037	-5.505832787	11.2803	0.1473	0.0095	0.02309	12.6551	0.06466	0.0217	0.0111	0.828948	0.288616	0.004103	0.002726	316.07	1.67	440.42
48	83.84501338	-5.527000855	12.2636	0.15405	0.01354	0.01051	14.4277	0.0801	0.063	0.00569	0.457653	0.073295	0.003914	0.001426	291.03	0.79	503.44
49	83.85831779	-5.429934619	11.3567	0.25637	0.0281	0.01127	14.955	0.0025	0.02352	0.00545	0.798198	0.042626	0.012866	0.000412	285.94	1.03	203.63
50	83.81740099	-5.415657407	12.3663	0.144	0.01447	0.02249	12.9353	0.07994	0.01686	0.02084	0.344818	0.218099	0.003521	0.001498	41.43	0.54	93.62
51	83.82657047	-5.407414011	12.9546	0.03889	0.02408	0.03683	13.3095	-0.0916	0.08866	0.03445	0.212993	0.146618	0.002143	0.003701	254.0	0.42	70.03
52	83.81419875	-5.433193235	13.5574	-0.18268	0.01932	0.00492	17.1937	-0.31123	0.03401	0.03388	0.128238	0.010471	0.000738	0.000182	91.71	1.57	157.45
53	83.81199692	-5.403242771	12.2095	0.03668	0.01502	0.00801	12.254	0.06378	0.00146	0.00032	0.439431	0.42074	0.004345	0.000387	336.22	1.34	54.29
54	83.81573332	-5.406840395	13.1448	0.08197	0.11398	0.00834	14.1365	-0.1525	0.21425	0.00495	0.172171	0.073254	0.0083	0.008503	84.78	0.25	62.63
55	83.80571344	-5.398079905	13.7532	-0.40305	0.00883	0.03132	14.3648	-0.36328	0.00074	0.00117	0.10579	0.064912	0.000391	3.3e-05	280.12	0.98	55.33
56	83.80291343	-5.452961783	12.5712	-0.0486	0.00591	0.0051	12.5777	-0.05039	0.01511	0.00762	0.300361	0.299461	0.000737	0.001895	21.52	0.27	234.7
57	83.71669487	-5.411941851	12.6526	0.07137	0.13295	0.02342	12.7138	0.16735	0.14902	0.02458	0.361068	0.346167	0.03348	0.034895	254.17	0.5	375.45
58	83.76820899	-5.387204813	11.3141	0.18785	0.07296	0.02795	12.2152	-0.18174	0.09618	0.00477	0.828116	0.389445	0.033476	0.025407	318.89	1.03	181.57
59	83.75430427	-5.402825758	11.9109	0.066	0.00149	0.00187	12.209	0.10544	0.00297	0.0015	0.483427	0.382948	0.000425	0.00079	247.41	1.05	236.2
60	83.74711256	-5.392456476	13.2541	-0.03134	0.01629	0.00829	13.8071	-0.03113	0.04928	0.03227	0.151572	0.100371	0.000789	0.002337	350.7	0.6	257.49
61	83.75085224	-5.402563056	14.8182	0.1399	0.01151	0.004	16.5954	-0.322	0.01252	0.01322	0.070804	0.019725	0.000326	0.000119	10.76	1.49	248.2
62	83.69329687	-5.408822911	11.6392	0.12523	0.01411	0.01518	13.1086	0.04691	0.01475	0.01212	0.68968	0.199359	0.006249	0.001087	274.14	1.48	456.27
63	83.6789671	-5.335279829	11.0598	0.12879	0.01307	0.02797	11.164	0.07703	0.11576	0.01705	1.085792	1.043077	0.007172	0.060041	351.92	0.27	539.42
64	83.73318716	-5.36862182	14.1939	-0.04466	0.02008	0.00515	14.3152	-0.0748	0.10923	0.06099	0.071881	0.067254	0.000491	0.004651	329.48	0.28	316.63
65	83.71736831	-5.375495097	11.0921	0.14235	0.26149	0.00092	11.4305	0.0573	0.27645	0.02362	0.917212	0.766359	0.214105	0.197388	213.64	0.41	367.93
66	83.71579716	-5.360911408	13.1125	0.00998	0.00071	0.01474	13.1251	-0.00467	0.14355	0.01523	0.218997	0.215652	6.2e-05	0.012077	12.53	0.44	384.25

NOTE—Table 2 is published in its entirety in the machine-readable format. A portion is shown here for guidance regarding its form and content.

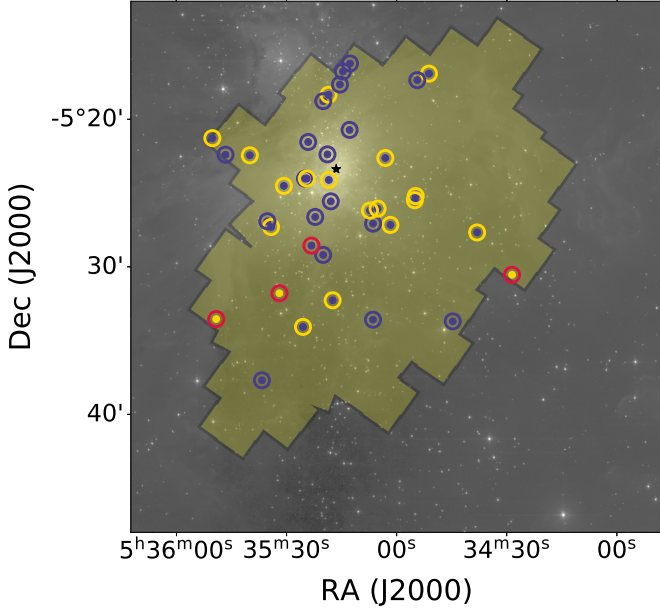


Figure 5. Large scale view of ONC. The shaded yellow area indicates the field covered by the WFC3 observations, overlaid on the 2MASS J-band image of the region (in grayscale). The black star marks the position of θ^1 Ori-C. Colored open circles and dots mark the positions of new candidate binary systems, where the dots refer to primary stars and the open circles refer to candidate companions. The colors encode the mass of the object: blue = stellar mass object, yellow = brown dwarf, red = planetary mass object.

In Figure 5 we show the position of each candidate cluster binary projected against the survey area of the WFC3 survey while Figure 6 shows the color magnitude diagram for the entire region with the locus of the KLIP candidate cluster binaries.

4.2. Wide binaries

Previously, binary systems that were well resolved in Catalog I were excluded from our analysis, which was designed to discern close companions hidden under the PSF wings of apparently single stars. We now expand our close companion catalog by adding the wider pairs from Catalog I – 58 systems with projected separation $d < 1.8''$ (choosing as limit the maximum distance at which we still measure an increase in the number density of stars – see Figure 8 in Section 4.4) and colors compatible with cluster membership for both sources. The brightest star of each pair is generally taken as the primary. Adopting the F130N filter photometry in Catalog I to estimate their masses, we obtain for the primaries values in the range $M_P = 0.02 - 1.08 M_\odot$, while for the companions we find $M_C = 0.01 - 1.04 M_\odot$. Their photometry and resulting physical parameters are listed in Table 2, and a gallery of images is shown in Figures

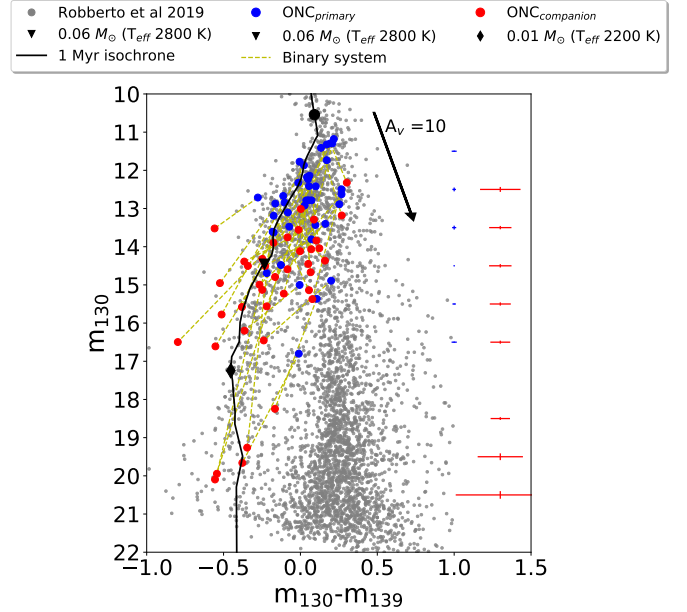


Figure 6. Recreation of the CMD from Figure 1, now including the candidate binary systems. The black line is the 1 Myr isochrone of Paper I, with three characteristic masses marked ($M_\odot = 0.02, 0.08$ and 1). The blue (red) crosses to the right show the average uncertainties for the primaries (companions) in each magnitude bin. The yellow dotted lines join the components of each candidate binary system.

19 in Appendix B (similarly to what we presented for the KLIP pairs).

It should be noted that we did not attempt to find faint substellar companions under the PSF wings of the Paper I binaries, as this goes beyond the current capabilities of our implementation of the KLIP algorithm. Our search strategy, therefore, is generally biased against finding triplets or higher order systems.

4.3. Master Catalog

Hereafter we will refer to the combination of Table 1 and Table 2 as to our Master Catalog. The Master Catalog contains 97 pairs of stars with separations between $0.16'' - 1.73''$ (corresponding to $66 - 697$ AU) and masses in the range $M_P = 0.015 - 1.27 M_\odot$ and $M_C = 0.004 - 1.04 M_\odot$ for the primary and companion, respectively.

Figure 7 shows the relation between primary and companion masses for all sources in the Master Catalog, with relative error bars and colors identifying the KLIP binaries (black) vs. Catalog I binaries (blue). The diagonal lines mark the loci of systems with primary mass equal to 1, 10 and 100 times the mass of the companion, whereas the horizontal and vertical lines indicate the boundaries between stellar, brown dwarfs and planetary

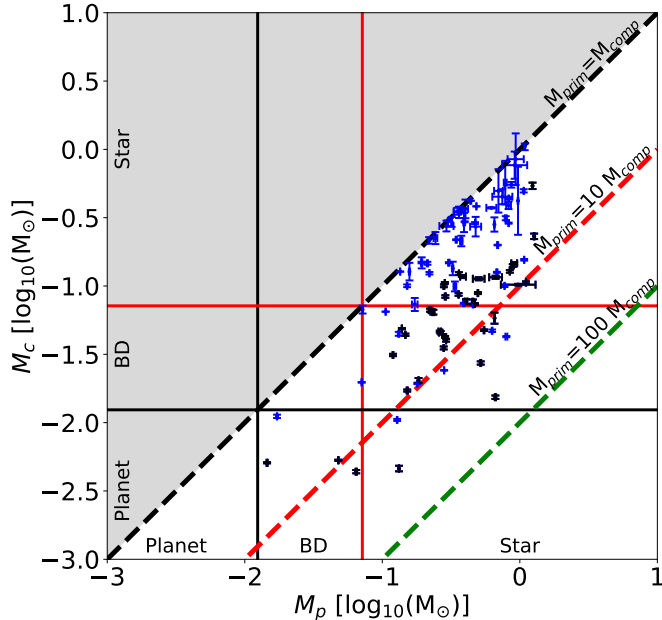


Figure 7. The plot shows the relation between mass of the companion and the primary for each candidate binary system, with blue indicating pairs found in Catalog I and black indicating pairs found in this work. The three dotted lines mark where $M_P = M_C$ (black dotted line), $M_P = 10 M_C$ (red dotted line), $M_P = 100 M_C$ (green dotted line). The planetary mass objects are separated from the brown dwarf mass objects with a black solid line while the brown dwarf mass objects and stellar mass objects are divided by a red solid line

mass objects. The number of systems in the areas delimited by these lines is given in Table 3. Overall we observe a primary star-to-brown-dwarf ratio (SBdR) $N(0.1-1.27 M_\odot)/N(0.014-0.07 M_\odot) = 15.16$, while the same ratio for isolated stars in the ONC (~ 3.8 evaluated from Catalog I or $3.3^{+0.8}_{-0.7}$ from Slesnick et al. 2004; Andersen et al. 2008) and in the field (5.2 or 6 from Bihain & Scholz 2016 and Kirkpatrick et al. 2012 respectively) is much smaller. Because the two SBdRs are different from each other (binaries vs singles in ONC/field), this may suggest a preference for companions to form around stellar mass primaries instead of brown dwarf in the ONC. This discrepancy may be due to the intrinsic difficulty in detecting companions around fainter primaries, so we evaluated the SBdR from our *completed* catalog of binaries obtaining $\sim 10.6 \pm 0.3$. Even if we consider the *completed* distribution of binaries, we still observe a preference for companions to form around primaries in the stellar mass regime compared to brown dwarf mass.

4.4. Crowding and apparent pairs

Given the increasing stellar density toward the inner regions of the cluster, one may expect to find apparent

Table 3. Summary of detections in Master Catalog.

		Primary		
		Star	Brown Dwarf	Planet
Companion	Star	63	-	-
	Brown Dwarf	26	2	-
	Planet	2	4	0

pairs due to chance alignments, i.e. cluster members that have small projected separation but are physically unrelated. Assuming a random distribution, one can use estimators like a two-point correlation function to evaluate the probability of observing a pair at a particular separation. Departures from random probability may indicate the presence of real close binaries.

To perform this analysis, we follow Jerabkova et al. (2019), building the so-called Elbow plot (Gladwin et al. 1999; Larson 1995), showing the number density of detected targets (Σ) as a function of the separation on-sky (θ). As shown by Gladwin et al. (1999), the presence of an elbow in this distribution graphically indicates the presence of resolved binaries.

Figure 8 shows the Elbow plot derived from the cluster selected isolated sources of Catalog I (black dash-dotted histogram) and the same data where we also add the *completed* distribution of binaries obtained from the Master Catalog (black solid histogram). To investigate how the excess of binaries varies with the radial distance from the cluster center, the figure also shows the results for four different rings centered around the position of θ^1 Ori-C. Overall the different distributions agree with each other, all showing a clear overabundance of multiple systems starting at $\sim 10^3$ AU (black vertical line). This result is in agreement with Scally et al. (1999) who suggested, based on a common proper motion study, that there should be no binaries wider than 1000 AU. Using GAIA DR2 data in combination with ground-based visible images, Jerabkova et al. (2019) finds for the ONC that the overabundance of multiple systems stars at ~ 3000 AU. Our data, reaching fainter objects with the diagnostic power to separate cluster members from background sources, lend support to Scally’s findings. Moreover, fitting the elbow part of the global $\Sigma(\theta)$ distribution we find a slope -1.98 ± 0.30 (red line), in excellent agreement with typical values for young clusters (Gladwin et al. 1999) as well as for early studies of the ONC in particular (Bate et al. 1998). These results indicate that the true population of binaries in the ONC has been reliably assessed, and that no overestimate is introduced by our completeness correction.

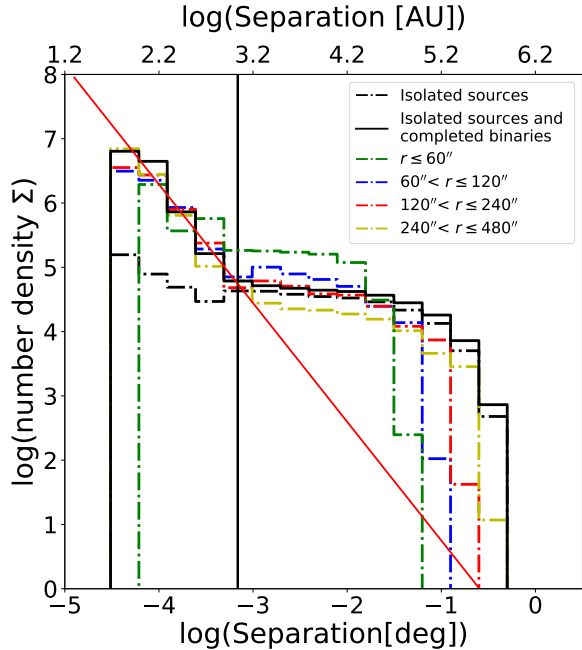


Figure 8. Elbow plot showing the number density of stars $\Sigma(\theta)$ as a function of the on-sky separation θ . The dash-dotted black histogram shows data from the cluster selected isolated sources from Catalog I (no binaries), while the solid black histogram shows the same data where we added the *completed* distribution of binaries obtained from the Master Catalog (isolated sources plus binaries). The colored dash-dotted histograms shows the distribution obtained from the isolated sources plus binaries data cut at different distances (r , in the legend) from the position of θ^1 Ori-C. The strong gap between the elbow of the isolated sources and the other ones shows that our binaries have to be bound. The vertical black line show the transition point between the flat portion of the $\Sigma(\theta)$ and the start of the elbow in our plot ($\sim 10^3$ AU). The red line shows the fit of the elbow for the completeness-corrected Master Catalog (slope: -1.85 ± 0.32).

4.5. Comparison with previous HST surveys

Reipurth et al. (2007), using HST/ACS H α images from GO-9825 with 50 mas pixel size (corresponding to about 20 AU, 2.5 times smaller than our WFC3-IR data) performed a major survey for visual binaries in the ONC probing a range of separations similar to ours. More recently, De Furio et al. (2019) used PSF fitting to find close pairs in HST/ACS F555W (V-band) images from GO-10246 to probe separations smaller than 160 AU. These surveys, like those performed using ground-based Adaptive Optics systems, in particular Duchêne et al. (2018), are complementary to our study as they target brighter and bluer (i.e. typically more massive) sources at smaller separations. Comparing the systems in our Master Catalog with those reported in the three afore-

Table 4. The table shows the number of matched binaries between our catalog and previous surveys. The columns shows the number of binaries matched to our Master Catalog (Cluster) or detected and rejected because a component was assigned to the background (Background), the number of binaries matched to a single star in Catalog I but not present in the Master Catalog (Unresolved) or not matched at all (Not Matched)

	Cluster	Background	Unresolved	Not Matched
Reipurth et al. 2007	53	16	8	14
Duchene et al. 2018	0	0	7	7
DeFurio et al. 2019	3	3	5	3

mentioned surveys, we obtain the results listed in Table 4. The columns list the number of targets we identify as cluster members (“Cluster”), those having at least one component classified as background source (“Background”), those appearing unresolved in our data even after KLIP processing (“Unresolved”), and those that do not match any source in our catalog (“Not matched”). If we exclude the binaries that were previously identified in Reipurth et al. (2007) and De Furio et al. (2019) and those identified in Paper I, we are left with 21 new candidate binaries uncovered by the KLIP algorithm. These new candidate detection span a range of primary masses between $0.014 - 0.127 M_{\odot}$, companion masses $0.004 - 0.23 M_{\odot}$, separations $0.16 - 0.76''$ and completeness between 17% – 87% with 49% as median value.

Figure 9 shows a comparison between the separations reported in our Master Catalog versus those given by Reipurth et al. (black) and De Furio et al. (red). Overall, there is excellent agreement between our values and those reported by these surveys, with only one major discrepancy against the Reipurth et al. catalog: their Source JW 638 is listed as having a companion at $\sim 1''$ separation, whereas our IR images (as well as the ACS visible images of Robberto et al. 2013) show a closer companion at separation $\sim 0.4''$ (see Fig. 17, ID 7). If we exclude this detection, the average scatter of separations between our catalog and the others is $\sim 0.05''$, less than 1/2 WFC3 pixel.

5. DISCUSSION

5.1. Binary Frequency

The multiplicity function (MF) of multiple systems is defined as:

$$MF = \frac{N_{mult}}{N_{mult} + N_{single}} \quad (5)$$

where N_{mult} and N_{single} are the number of multiple and single star systems in the sample. In Table 5 we report

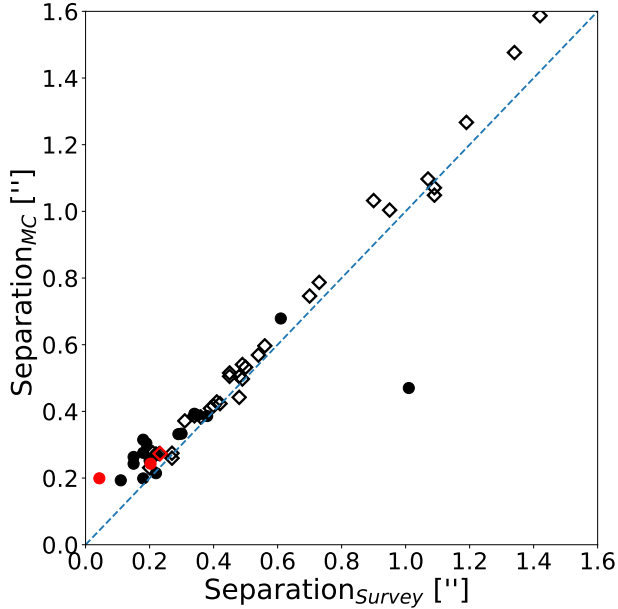


Figure 9. Comparison of separation between Reipurth et al. (black) and De Furio et al. catalogs (red) vs *Master Catalog* for matched cluster-cluster binaries. The dots mark the position of the matched binaries obtained through KLIP PSF subtraction, while the hollow diamond marks the matched binaries obtained from Paper I. The blue dotted line shows the locus of point where $\text{Separation}_{\text{ONC}} = \text{Separation}_{\text{Survey}}$

the MF values for a) the Master Catalog (“all”); b) for the Master catalog split in two different bins of primary mass (“star or ”BD”), and c) three different primary mass bins (B0, B1 and B2) having the same number of systems in each bin. Table 5 shows that the fraction of binaries among stellar mass objects is 3 times larger than among substellar mass objects, for the separation range we are considering. The deficit of very low mass binary systems remains regardless on how the limits are defined, as shown by the bottom half of the table.

A variety of MF values have been previously reported in the literature for the ONC. Petr et al. (1998) looked for binaries in the inner $40'' \times 40''$ around the Trapezium, finding $MF = 5.9\% \pm 4.0\%$ in the separation range $0.14'' - 0.5''$ (63-225 AU). In a similar separation range we obtain $MF=8.1\% \pm 0.8\%$. Köhler et al. (2006) performed a survey of the periphery of the ONC at 515 arcmin (0.652 pc) from the cluster center, probing separations from $0.1'' - 1.2''$ and primary masses from $0.1 - 2 M_{\odot}$, finding $MF=5.1\% \pm 2.7\%$; for a similar range of mass and separation we find $MF = 13.0 \pm 1.1$. Reipurth et al. (2007) report $MF=8.8\% \pm 1.1\%$ in the range of separations $0.17'' - 1.69''$ (67.5 – 675 AU) while

Table 5. Multiplicity Fraction (MF) for the complete sample (first row) and different subsamples of primary masses in separation range of $0.16''$ - $1.73''$.

Label	Primary mass [M_{\odot}]	MF [%]
All	0.01-1.27	11.5 ± 0.9
Star	0.08-1.27	14.6 ± 1.1
BD	0.01-0.08	4.6 ± 1.3
B0	0.50-1.27	21.6 ± 2.9
B1	0.28-0.50	14.5 ± 1.9
B2	0.01-0.28	6.8 ± 1.0

we find $10.8\% \pm 0.9\%$. In general, we obtain larger MF values than previous ONC studies because the combination of *HST*/WFC3 and KLIP allows us to unveil a larger number of faint companions at low angular separations. Still, in comparison with other star forming regions, our multiplicity function is ~ 2 smaller than e.g. Taurus over a similar separation range (Duchêne & Kraus 2013). On the other hand, comparing our result with the binary frequency in the field obtained by Duquennoy & Mayor (1991) for a similar range of separations, we find approximately the same binary frequency between the field and the ONC. This result is also in agreement with De Furio et al. (2019) where the author find that the low-mass star binary population of ONC is consistent with that of the Galactic Field over mass ratio $0.6 - 1$ and separation $30 - 160$ AU.

5.2. Binary Separation

The left panel of Figure 10 shows the distribution of projected separations in the Master Catalog in bins of $0.3''$ before and after completeness correction. The right panel shows histograms of the separations for the three equally populated mass intervals B0, B1, B2 introduced in Section 5.1. Overall, the separation distribution is peaked toward small values $\lesssim 0.6''$, or 240 AU. At larger distances, the distribution shows a plateau, both results being consistent with what has been already reported by Reipurth et al. (2007).

Spurzem et al. (2009) have analyzed the disruption of planetary systems in the ONC. Their numerical simulations indicate that moderately close stellar encounters can cause the disruption of planetary systems. They find that the ejected planets have typically low velocity dispersion and in young clusters can be retained by the cluster potential and appear as free floaters. Table 6, based on Spurzem et al. (2009) Eq. 36 and Eq. 37, shows the typical timescale to get a free floater (τ_{ff}) for the “close” ($0.1'' - 0.6''$) and “wide” ($0.6'' - 1.5''$)

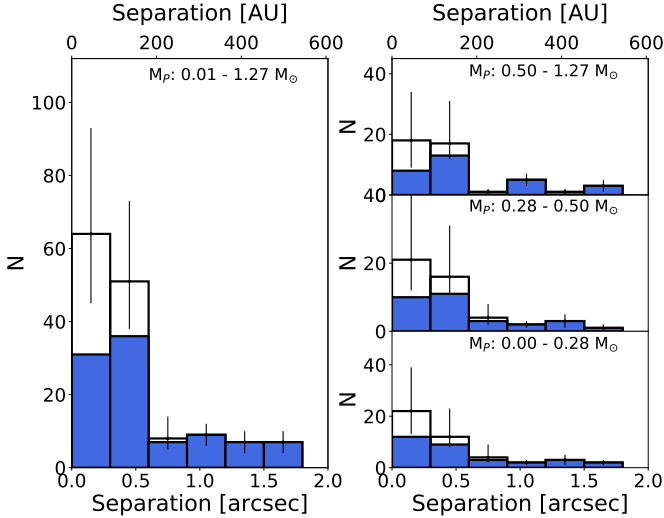


Figure 10. Separation distribution for our full sample (left) and different subsamples of primary masses as in Table 5, in bins of $0.3''$. The number of observed companions in each bin is given by the blue histogram; the hollow black histogram – as before – indicates the completeness-corrected value. Error bars are determined according to Poisson statistics.

Table 6. Typical timescale for free floaters for the close and wide binary populations

	Primary mass	Companion mass	Separation	τ_{ff}
	$[M_{\odot}]$	$[M_{\odot}]$	$['']$	$[Myr]$
close	0.45	0.22	0.32	111
wide	0.36	0.17	1.13	37

population of binaries assuming our typical values for the primary and companion mass, and system separation. Considering the total number of systems that may harbor a companion, disruptions can be expected, in particular for the wide binary population in the central region of the cluster which had statistically enough time to undergo at least one strong gravitational encounter. The observed spectrum of binary separations, in particular the discontinuity between close and wide binaries at $0.6''$ (240 AU), can thus be attributed to stellar encounters, as anticipated by Reipurth et al. (2007).

5.3. Binary Separation vs. Distance from the Cluster center

In this section we examine if the close and wide binaries, separated at 240 AU, can be isolated as two distinct populations depending on the distance from the cluster core.

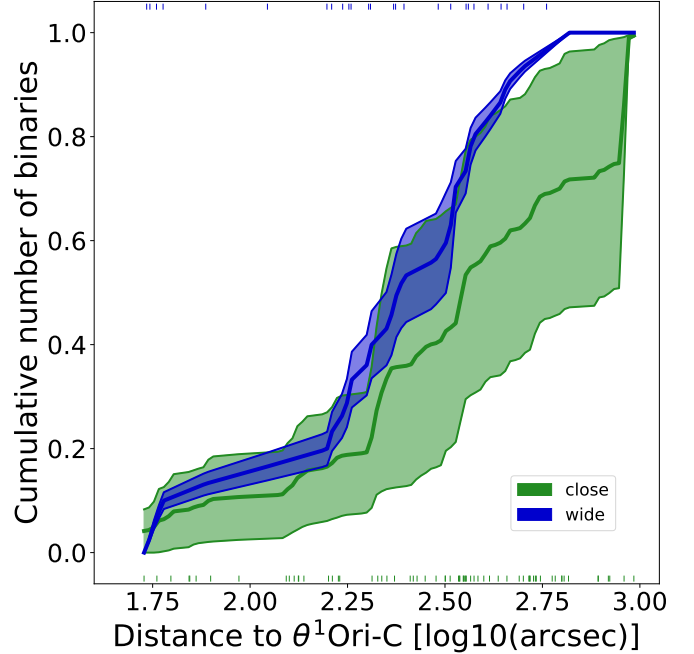


Figure 11. The green (blue) area shows the family of curves obtained through the simulations of *completed* (see text) cumulative distribution for close (wide) binaries as a function of the distance from $\theta^1 Ori$. The green (blue) vertical ticks at the bottom (top) of the plot show the distance from the core for each system used to generate the synthetic populations.

To perform this analysis, we study the completeness-corrected cumulative distributions of close and wide binaries, but instead of simply applying a completeness correction to our observations, we estimate the “true” number of underlying objects required to observe an object given the estimated completeness \mathcal{C} . The number of missed detections for each successful detection at completeness \mathcal{C} is modeled as a negative binomial distributions representing the number of failures f occurring before a number of successes s is observed, assuming a probability p of single success. We define the specific shape of the negative binomial distribution (for each detection) by using the value $p = \mathcal{C}$ for the individual trial success probability, and $s = 1$. Using this negative binomial distribution, we extract a random number of “failures”, i.e. undetected companions, that were not observed due to noise and/or incompleteness. We then assign to each of these systems a distance from the center similar to that of the actually observed systems. Finally, we iterate over the sample of observed binaries to obtain a single realization of a “complete” binary population and repeat this procedure one thousand times to obtain the *completed* cumulative distributions shown in Figure 11 for close (green) and wide (blue) binaries. For each iteration we perform a 2-sample Kolmogorov-

Table 7. Fitted values for Γ in the broken power law in the mass range $0.015 - 1.27 M_{\odot}$.

Group	Γ_1	Γ_2	$\log M$
Primaries	-0.9 ± 0.5	0.2 ± 0.4	-0.3 ± 0.1
Companions	-0.6 ± 0.7	0.9 ± 0.6	-0.8 ± 0.2

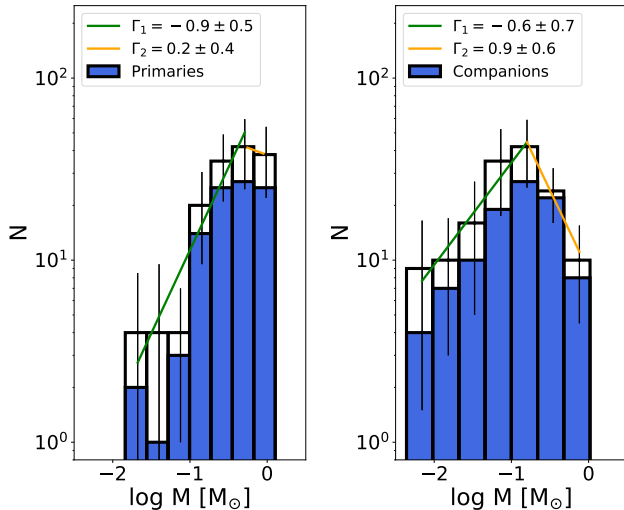


Figure 12. Histogram of masses for primaries and companions. The blue histogram shows the number of companions, while the hollow histogram is corrected for completeness. To bin the two distributions we used *Scott’s method* (Scott 1979), where the optimal histogram bin width takes into account data variability and data size by asymptotically minimizing the integrated mean square error.

Smirnov test (KS-test) on the *completed* populations of close and wide binaries as a function of the distance from the core of the cluster. For $\sim 48\%$ of the KS-tests we obtain a p-value below 0.01. At this level of confidence, we can not safely reject the hypothesis that the two samples are drawn from the same distribution. This suggests that the two populations may be different with respect to their spatial distribution.

5.4. Mass distribution

In order to probe the Initial Mass Function of multiple systems, in Figure 12 we show the histograms of the primary and companion masses. We fit the histograms using broken power laws (i.e. $\sim m^{-\Gamma_i}$), adopting the peak of each specific sample as the breaking point, obtaining the results shown in Table 7. Even though the values of Γ_1 are compatible within the errors, both the Γ_2 and the peak of the two populations is not compat-

ible within 1σ . To further characterize the possible differences between the mass distributions of primaries and companions and how they compare to the mass distribution of single stars in the ONC, we show in Figure 13 a set of cumulative mass distributions obtained following the same procedure introduced in Section 5.3. The top left panel shows the comparison between single systems, primaries and companions. The top right panel shows the comparison between single systems and the full set of masses, both primaries and companions taken individually (we refer to this joint set of mass values as ”union”). The bottom panel shows the same comparison where we coadded the mass of the two components of each pair (we refer to this set of mass values as ”sum”). In each plot we also show the cumulative distribution obtained from a Kroupa IMF (Kroupa 2001), a Chabrier IMF for single objects (Chabrier a: eq. 17 in Chabrier 2003), a Chabrier IMF with unresolved binaries (Chabrier b: eq. 18 in Chabrier 2003). To avoid introducing biases due to the saturation limit of our survey, we cut the mass distributions at $1 M_{\odot}$. As explained in Sec. 5.3, we generate one thousand *complete* samples for each population. For each combination we perform a 2-sample KS-test. The results, summarized in Table 8, are characterized by the ratio $n = \frac{n_i}{n_{tot}}$ where n_i is the number of times the KS-test provides a p-value ≤ 0.01 (corresponding to a confidence level $> 99\%$ that the two population are distinct) and n_{tot} is the total number of simulations. As the ratio increases, it is safer to reject the hypothesis that the two samples are drawn from the same population. The results suggest that the populations are generally different, in particular a) the mass distribution of the binaries is different from the mass distribution of single stars, b) both are different from the Kroupa/Chabrier IMFs, and c) the primary and companion mass distributions are different from each other (as already noted in Fig 12). The ”union” mass distribution is compatible with a Chabrier IMF with unresolved binaries in $\sim 31\%$ of the tests. The ”sum” mass distribution is always incompatible with any Kroupa/Chabrier IMFs.

We interpret these inconsistencies as a result of a systematic deficiency of companion detections below 100 AU. Regardless of our best efforts and of our advanced detection techniques, the technical limit of 1-2 pixels for the closest resolvable pairs is basically insurmountable.

Although in this simple exercise we try to enhance the number of binaries by making use of our completeness tests, it must be remarked that the enhancement is only partial. For every detected binary we can compute the chance for that binary to be detected at exactly the separation and magnitude contrast at which it is detected, and we can enhance our sample by one

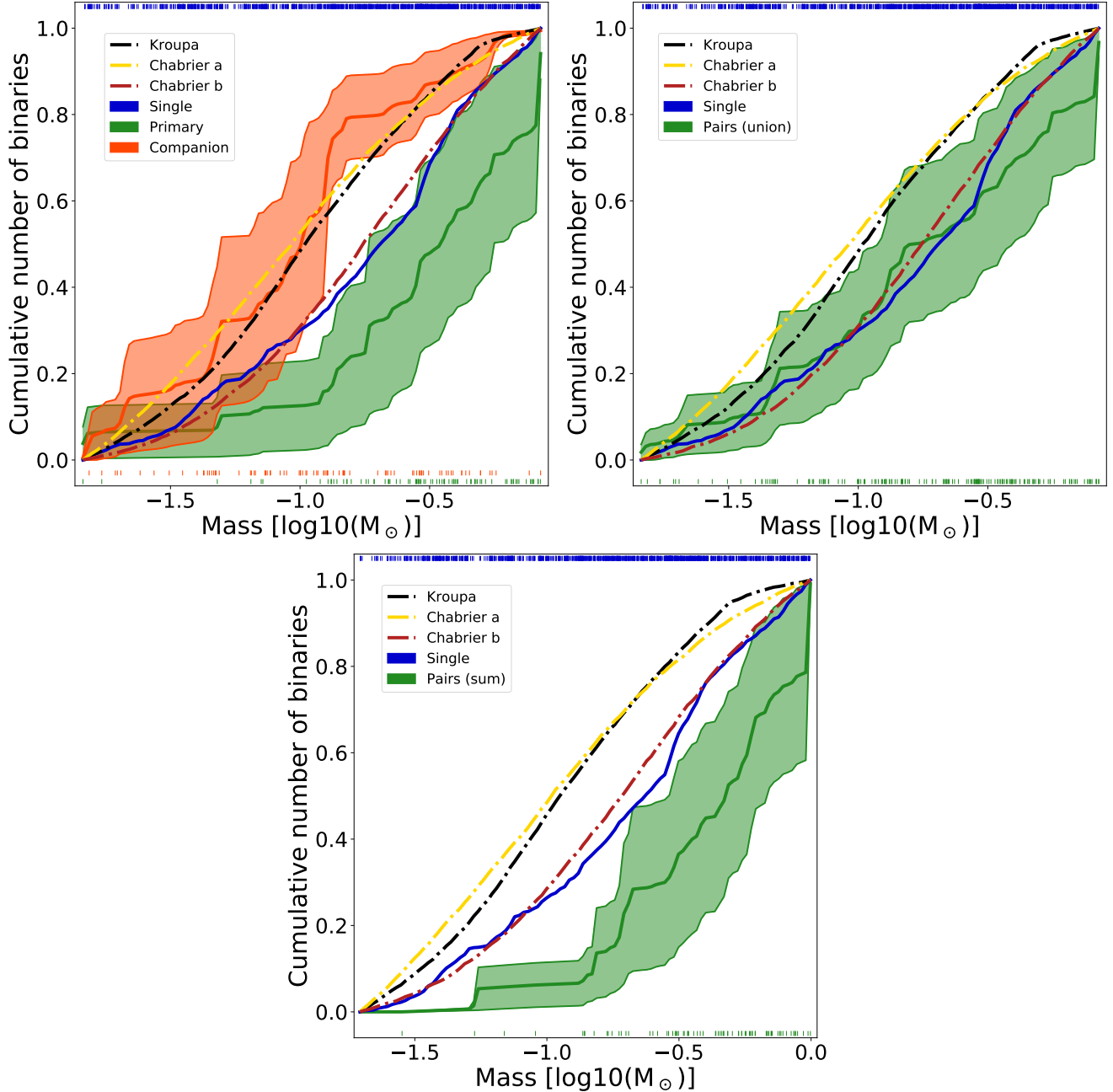


Figure 13. Families of curves obtained through the simulations of *completed* cumulative distributions, as explained in the text. Also shown for reference are the cumulative distributions obtain from a Kroupa IMF (dash-dotted black line), a Chabrier IMF for single systems (Chabrier a: dash-dotted yellow line), and a Chabrier IMF with unresolved (Chabrier b: dash-dotted brown). The colored vertical ticks at the top and bottom of the plot show the total mass of each system used to generate the synthetic populations.

minus that chance. However, we cannot account for the truly undetected binaries (i.e., the truly close pairs and those with high flux contrast). A demonstration of this is that our "Single" stars sample (blue line in the top left panel of Figure 13 follows the distribution of stellar systems (including unresolved binaries) by Chabrier

(2003), an obvious sign that many binaries are actually hiding within our singles.

For the same reason, even the the conclusions on dissimilarities of the mass distribution of primaries and companions in detected pairs can only be partial, due to biases affecting which systems are preferentially detected as such.

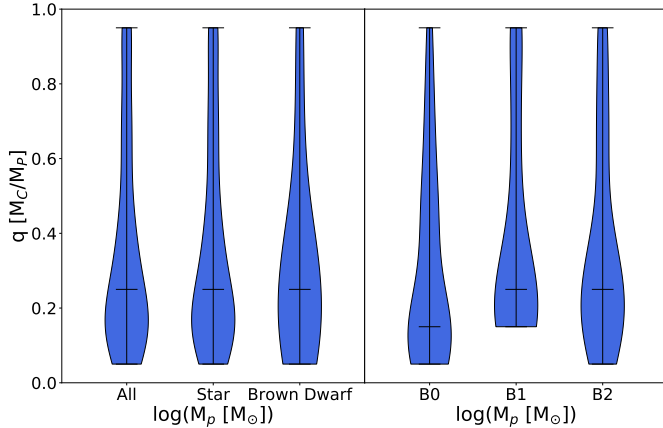


Figure 14. Left panel: violin plots of the mass ratio distribution for all candidates and candidates with primaries in the stellar/brown dwarf mass regime. Right panel: same as left panel for different bins of mass of the primary (see the Table 9 for more details). The shape of each distribution show the probability density of the data smoothed by a kernel density estimator while the horizontal black lines mark the median value for each of them

A more complete exercise, involving modeling the a-priori binary mass distribution, SMA, inclinations, eccentricity and spatial distribution within the cluster will be the focus of an upcoming paper in this series (Pueyo et al, in preparation).

5.5. Mass ratio

In this final section we analyze the mass ratio distribution $q = \frac{M_C}{M_P}$, grouping binaries in different bins according to the mass of the primary and following the classification adopted to produce Table 5. The results are shown as violin plots (i.e. a method for graphically depicting groups of numerical data similar to a box plot with a marker for the median of the data and the addition of a rotated kernel density plot on each side). Overall, we obtain a median value for the mass ratios $q \sim 0.25$, indicating a deficiency of similar-mass binaries (which would have $q \sim 1$). This result is in agreement with what reported by Duchene et al. (2018) for smaller separations (10-60 au). To compare our results with others work, we characterize the distribution of mass ratio as a power law $f(q) \propto q^\gamma$. Fitting the completeness-corrected histogram, we determine the median values of q and γ reported in Table 9, for the different mass bins. From a theoretical point of view we would expect that binaries with separation $\lesssim 100$ AU most likely have formed through fragmentation of the protostellar disk while wider systems via free-fall fragmentation during early collapse. Because these two process occur at different times and through different mechanics, it's rea-

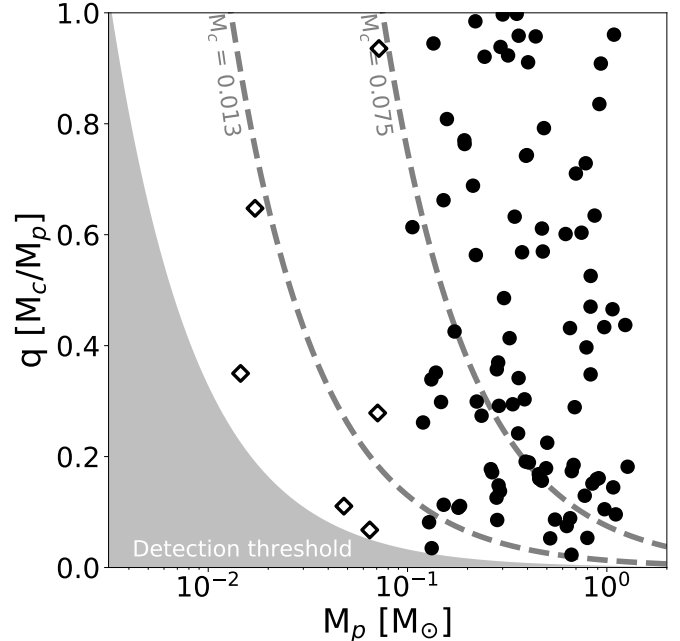


Figure 15. Distribution of mas ratio as a function of mass of the primary for the *ONC candidate binary catalog* objects. The primary masses for each candidate are shown by their shape (circle = star; hollow diamond = brown dwarf). The two grey dashed and dot dashed lines show the values of q for which $M_c = 0.075$ and $M_c = 0.013$ as a function of M_p

sonable to expect them to produce companions with different mass functions and in turn different distribution of mass ratios. We tested this hypothesis obtaining $\gamma_{\lesssim 100 \text{ AU}} = -1.1 \pm 0.5$ and $\gamma_{\gtrsim 100 \text{ AU}} = -0.6 \pm 0.2$, finding that the distribution whit separation $\gtrsim 100$ AU (with a bigger and better constrained sample) is incompatible at 2.5σ from the population of binaries with separation $\lesssim 100$ AU.

Correia et al. (2013) studied eight adaptive optics spatially-resolved binaries in the ONC (along with seven binaries from the literature) in separation range 85–560 AU and primary mass 0.15–0.8, finding $\gamma = 1.03 \pm 0.66$, $\gamma = 1.11 \pm 0.37$ and $\gamma = 0.57 \pm 0.38$ for the B98, PS99 and S00 pre-main sequence tracks, respectively. The author find good agreement between their results in the ONC and other star forming regions (e.g. Taurus-Auriga), while our results seems to disagree with both (see below about our comparison with Taurus-Auriga). We think this discrepancy can be explained by the small number of candidates adopted in their survey and in the large amount of close-in small mass companion detected in ours. We decided to test this assumption down-sampling the number of candidates in our catalog, randomly extracting the same number as in Correia et al. in a similar range of masses and separation $\gtrsim 100$ AU. We re-

Table 8. Comparison between different samples. The table show the ratio n of KS two sample test providing a p-value below 0.01 over the total number of simulations. Bigger n allow us to safely reject the hypothesis that the two samples of each tests are drawn from the same population.

	Kroupa	Chabrier a	Chabrier b	Singles	Companions
Primaries	1	1	1	1	1
Companions	0.94	0.92	1	1	-
Pairs (Union)	1	1	0.69	0.79	-
Pairs (Sum)	1	1	1	1	-

Table 9. Median value of q and power-law index γ obtain for different range of mass of the primary.

Label	q -median	γ
All	0.25	-0.7 ± 0.2
Star	0.25	-0.7 ± 0.2
BD	0.15	-0.9 ± 0.8
B0	0.15	-0.8 ± 0.4
B1	0.25	-0.5 ± 0.3
B2	0.30	-0.6 ± 0.3

peated this operation one hundreds times finding that in 88%/78%/38% of the cases we agree within 2σ with the results from PS99/S00/B98 tracks. It is worth to notice that the candidate we exclude for this test have average completeness value of 76%, and any candidate with completeness smaller than 30% have been detected through multiple visits. So we conclude that the discrepancy can be attributed to the presence of close in small mass candidate companion we detected through KLIP analysis in our work.

Kraus et al. (2011) conducted a high resolution imaging survey of the Taurus-Auriga star forming region probing the range of separations between 15 – 5000 AU, primary and companion masses in the range 0.25 – 2.5 M_{\odot} and 0.01 – 1.17 M_{\odot} , respectively, obtaining $\gamma = 0.2 \pm 0.2$ at separation $\lesssim 100$ and 0.08 ± 0.2 at separations $\gtrsim 100$, i.e. finding an almost flat distribution of q with at most a slight excess of similar mass binaries. Instead, we find an overabundance of low- q binaries. This result still holds even if we consider a range of overlapping primary and companion masses and separations between the two surveys (0.28 – 1.27 M_{\odot} and 0.01 – 1.04 M_{\odot} and 66 – 680 AU respectively), obtaining $\gamma_{Kraus} = 0.3 \pm 0.3$ and our $\gamma = -0.4 \pm 0.2$. If instead we limit both dataset at separation $\gtrsim 100AU$ ad com-

panion masses $\gtrsim 0.05 M_{\odot}$, the gamma obtained from the two surveys are now compatible within $\sim 1\sigma$, reconciling the difference. Kraus et al. (2011) also remark that their mass-ratio distribution is in stark contrast with Duquennoy & Mayor (1991), who studied field binaries with spectral type between F7 to G9 spectral type ($\sim 0.8 - 1.4 M_{\odot}$) and found a mass-ratio distribution peaked towards low masses ($q \sim 0.3$) with few similar mass companions, a finding very close to our result, $q \sim 0.25$. They derived the γ from the Duquennoy & Mayor (1991) dataset, obtaining $\gamma_{q:0-1.1} = -0.36 \pm 0.07$ and $\gamma_{q:0.2-1.1} = -1.2 \pm 0.2$. This last value, obtained with a stronger fit $-\chi_{\nu} = 0.7$ with 7 degrees of freedom, is in good agreement with the γ we obtain for close in companions (separation $\lesssim 100$ AU) and for primary masses 0.5 – 1.27 $M_{M_{\odot}}$ (labeled 'B0' in Table 9). These results, together with the results about the multiplicity fraction presented in Sec. 5.1, suggest that ONC binaries may represent a template for the typical population of field binaries, upholding the hypothesis that the ONC may be regarded as a most typical star forming region in the Milky Way.

Figure 15 shows the mass ratio of each pair vs. the mass of the primary, i.e. the detailed distribution of the data points used to create Figure 14. The shape of each point indicates the mass of the primary (circle = star; hollow diamond = brown dwarf). The limits for substellar and planetary mass companions are shown as dashed lines. The gray area represents the region of parameter space inaccessible due to our detection limits. Figure 15 shows an overabundance of companions around stellar vs. brown dwarf primaries, consistent with the general trend for star forming regions and young associations (Duchêne & Kraus 2013). When detected, very-low mass companions tend to have $q \leq 0.4$. If present, very-low mass binary systems with nearly equal mass must have remained unresolved, with a projected SMA smaller than our inner separation limit at the distance of the Orion Nebula. In fact, Winters et al. (2019) find the majority of VLM objects in a local volume 25 pc radius

have $q \gtrsim 0.4$ and their separation peaks at ~ 20 AU. As a comparison, the smallest separation we resolve is $\simeq 50$ AU with low completeness $\mathcal{C} \sim 0.1$. On the other hand, our data seem to suggest that very-low mass binary systems with nearly equal mass and wide separation are exceptionally rare, a possible indication that core fragmentation at the lowest masses favors the formation of asymmetrical systems.

6. CONCLUSION

We performed a new analysis of *HST* WFC3/IR images of the Orion Nebula Cluster using the Karhunen-Loève Image Projection (KLIP) algorithm to find faint companions around low-mass primaries. Starting from a sample of 1392 unique bona-fide cluster targets, we find:

- 39 candidate binary systems within separation $0.16'' - 0.77''$ and mass range $M_p \sim 0.015 - 1.27 M_\odot$ for the primary and $M_c \sim 0.004 - 0.54 M_\odot$ for the companion. Of these, 21 are detected for the first time ever. The detection of the H_2O absorption feature allows us to assess with high confidence the membership of these sources in the ONC, although final confirmation of their nature as gravitationally bound systems will require future proper motion studies;
- the overall multiplicity fraction for the ONC determined from the HST/WFC3-IR data, is $11.5\% \pm 0.9\%$. In comparison with other star forming regions, this value is ~ 2 times smaller than e.g. Taurus over a similar separation range (Duchêne & Kraus 2013). We find approximately the same binary frequency in the field and in ONC (Duquennoy & Mayor 1991);
- the mass distribution of the sources belonging to a binary system (either primaries, companions, or combined) is different from the mass distribution of single stars; the primary and companion mass distributions are also different from each other;
- the mass ratio distribution is compatible with what expected from a scenario where close in binaries formed through fragmentation of the protostellar disk while wider systems formed via free-fall fragmentation; and
- an almost complete absence of brown dwarfs and VLM M-dwarfs pairs with similar mass (high- q systems), and a steep distribution of mass ratios peaked towards small q -values (median values $q \simeq 0.25$).

Overall our results suggest that ONC binaries may represent a template for the typical population of field binaries, supporting the hypothesis that the ONC may be regarded as a most typical star forming region in the Milky Way.

APPENDIX

A. RECEIVER OPERATING CHARACTERISTIC CURVES

A Receiver Operating Characteristic (ROC) curve is a plot that shows the diagnostic ability of a binary classifier system as the discrimination threshold (T) varies. The ROC curve is created by plotting the true positive rate (or TPR) versus the false positive rate (FPR) at various threshold T values. When T is set low enough, we accept the whole distribution of TP, but we also accept the whole distribution of FP, so in the ROC curve plot we are at the point (1,1). When we increase T , we will lose some TP as well as some FP (the exact rate and so the shape of the ROC curve depend on the exact distribution of the two populations) until we reach the point (0,0) where the selected threshold excludes all the TP and FP.

To build ROC curves for our detection we first need to simulate the TPR and FPR population representative of each of our candidates. Our sensitivity strongly depends on the magnitude of the primary (m_{F130M}), the contrast (Δmag) achieved by PSF subtraction, and the distance of the companion from the primary (separation). We therefore sorted our targets into magnitude bins of the primary from 10 to 22, Δmag from 0 to 10 (both with a width equal to 1) and separation from $0''$ to $1''$ in step of $0.1''$. To build the TPR distribution and the FPR distribution for each of these configurations:

- we created one thousand fake binaries. To simulate both the primary and the companion component, we first simulated an isolated star using the model of the PSF obtained from KLIP, re-scaled to match the flux of the object we want to simulate. To perturb the PSF model, we created a local model of the noise combining WFC3 error maps from all the stars of the survey in the same magnitude bin of the simulated star. To take into account different pixel phases we add a small shift (≤ 0.5 pixel) to the position of the star. Then we inject the simulated companion in the tile of the simulated primary and add the sky to the final combined tile. During this procedure we also saved the tile of the isolated primary for future analysis.
- for each simulation (either the binary or the isolated primary), we perform the same PSF subtraction process illustrated in Section 3.2, retrieving the value of the (positive) signal to noise ratio (SNR) in the pixel where we injected (building the TPR) or did not inject the companion (building the FPR). We decided to use only the positive values to build the ROC curves because by definition the signal from a candidate detection has to be positive.

To encapsulate in a single number the performance of our model to distinguish between classifier, we evaluate the Area Under the Curve (AUC) of an ROC. The higher the AUC, better the model is at distinguishing between the true positive population and the false positive population.

Figure 16 shows examples of the TP (blue) and FP (orange) histograms for a given binary configuration, and the corresponding ROC curve. Also provided for each ROC curve is the value of the corresponding AUC.

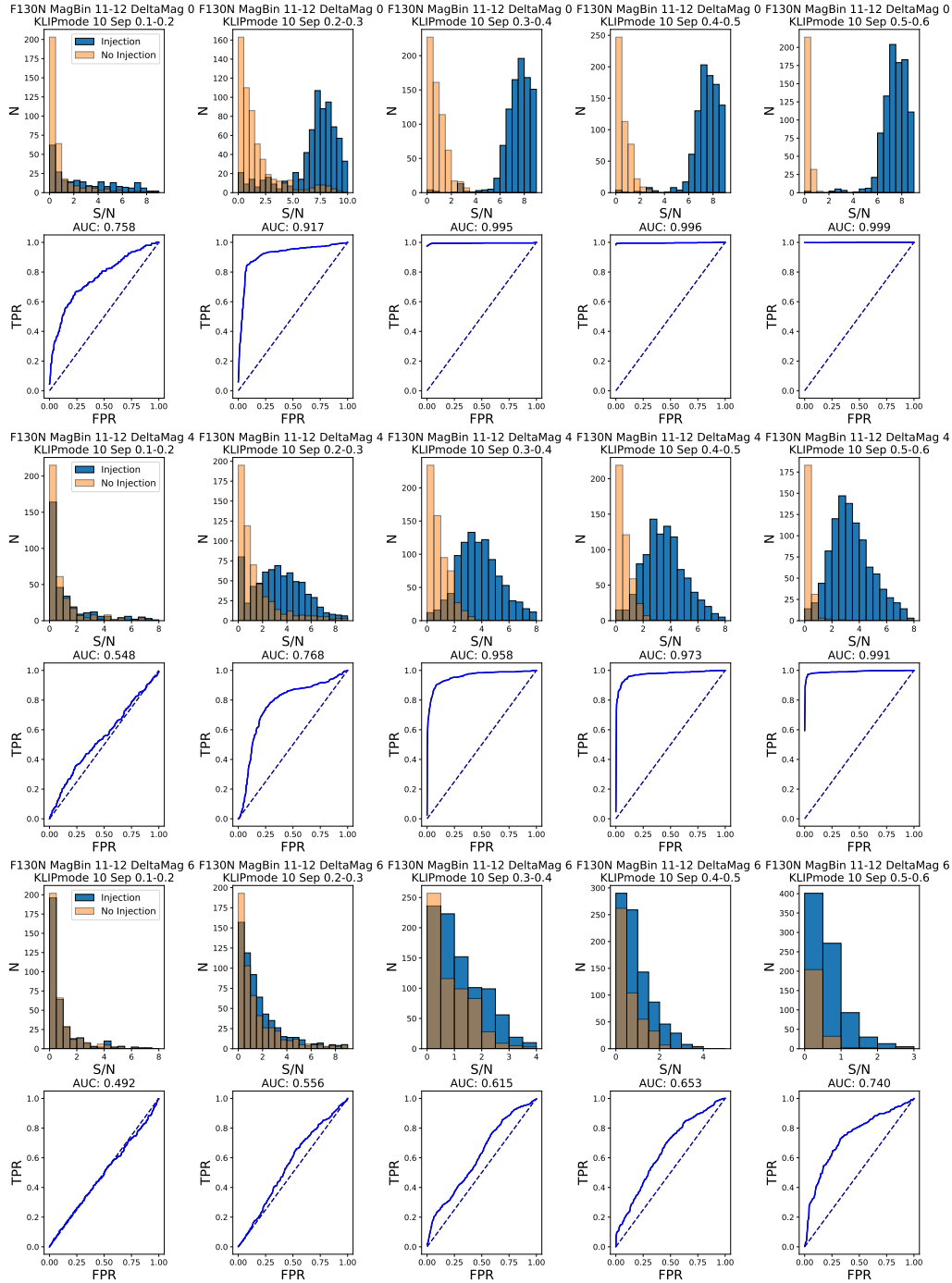


Figure 16. Distributions of signal to noise and derived ROC curves for filters F130N, magnitude bin of the primary 11-12, Δmag 0,4 and 6 and different distances from the center of the tile.

B. GALLERY OF BINARIES

Figures 17 - 18 show the coadded images pre- and post-subtraction for each of the candidate cluster binary presented in Table 1. Each stamps has a dimension of $2'' \times 2''$. Figure 19 shows the postage for the candidates binary from Table 2. Each stamps has a dimension of $2'' \times 2''$. Each postage stamp has been rotated and aligned to have North up and East to the left.

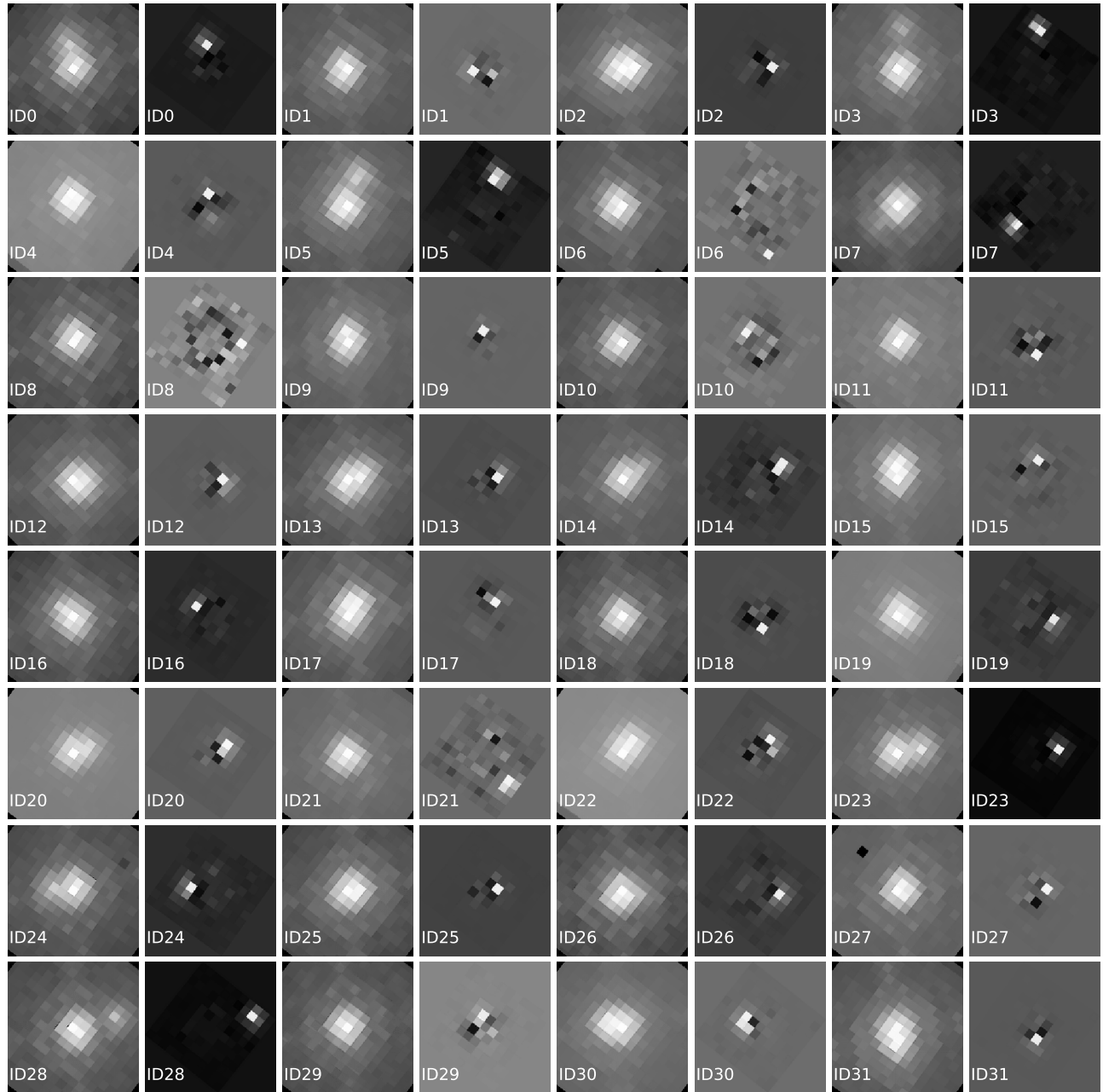


Figure 17. Each tile shows the residual image after running KLIP for each primary target for which we detect a companion (brighter pixel in the tile). Each stamps has a dimension of $2'' \times 2''$. The north is up and east is on the left

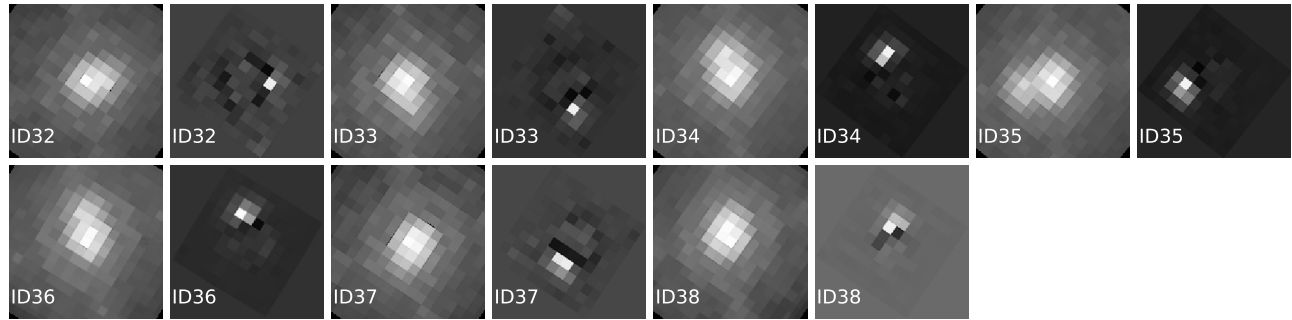


Figure 18. Each tile shows the residual image after running KLIP for each primary target for which we detect a companion (brighter pixel in the tile). Each stamps has a dimension of $2'' \times 2''$. The north is up and east is on the left

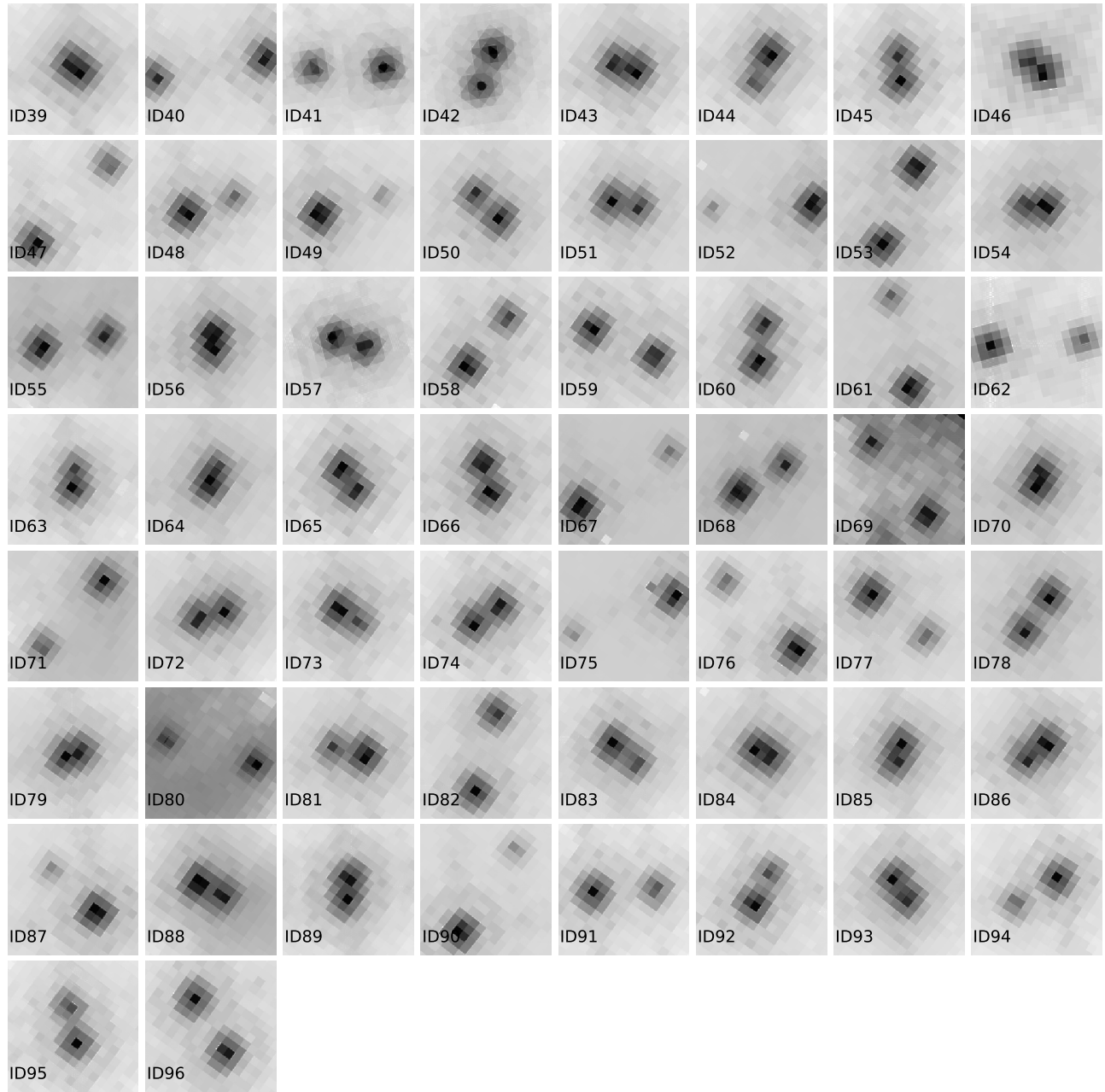


Figure 19. WFC3 binaries identified from Catalog I up to separation $\leq 1.5''$. Each stamps has a dimension of $2'' \times 2''$. The north is up and east is on the left

ACKNOWLEDGMENTS

The authors thank the anonymous referees for the interesting suggestions and comments. G. M. Strampelli wants to thank the Instituto de Astrofísica de Canarias for hospitality. The authors thank Bo Reipurth for useful comments on the manuscript. Support for Program number GO-13826 was provided by NASA through a grant from the Space Telescope Science Institute, which is operated by the Association of Universities for Research in Astronomy, Incorporated, under NASA contract NASS-26555. CFM acknowledges an ESO fellowship. JA was supported in part by a grant from the National Physical Science Consortium. GMS and AA are supported by the Ministerio de Ciencia, Innovación y Universidades of Spain (grant AYA2017-89841-P) and by the Instituto de Astrofísica de Canarias. This research has made use of the VizieR catalogue access tool, CDS, Strasbourg, France. The original description of the VizieR service was published in *A&AS* 143, 23.

Facilities: *HST* (ACS, WFC3)

Software: Numpy (van der Walt et al. 2011), Astropy (Astropy Collaboration et al. 2013; Price-Whelan et al. 2018), Scipy (Virtanen et al. 2020), Matplotlib (Hunter 2007), PyKLIP (Wang et al. 2015), Pandas (McKinney et al. 2010)

REFERENCES

- Andersen, M., Meyer, M. R., Greissl, J., & Aversa, A. 2008, *ApJL*, 683, L183, doi: [10.1086/591473](https://doi.org/10.1086/591473)
- Astropy Collaboration, Robitaille, T. P., Tollerud, E. J., et al. 2013, *A&A*, 558, A33, doi: [10.1051/0004-6361/201322068](https://doi.org/10.1051/0004-6361/201322068)
- Baraffe, I., Chabrier, G., Allard, F., & Hauschildt, P. H. 1998, *A&A*, 337, 403, <https://arxiv.org/abs/astro-ph/9805009>
- Bate, M. R., Clarke, C. J., & McCaughrean, M. J. 1998, *MNRAS*, 297, 1163, doi: [10.1046/j.1365-8711.1998.01565.x](https://doi.org/10.1046/j.1365-8711.1998.01565.x)
- Bihain, G., & Scholz, R. D. 2016, *A&A*, 589, A26, doi: [10.1051/0004-6361/201528007](https://doi.org/10.1051/0004-6361/201528007)
- Brandt, T. D., McElwain, M. W., Turner, E. L., et al. 2014, *Astrophysical Journal*, 794, doi: [10.1088/0004-637X/794/2/159](https://doi.org/10.1088/0004-637X/794/2/159)
- Chabrier, G. 2003, *PASP*, 115, 763, doi: [10.1086/376392](https://doi.org/10.1086/376392)
- Choi, J., Dotter, A., Conroy, C., et al. 2016, *The Astrophysical Journal*, 823, 102, doi: [10.3847/0004-637x/823/2/102](https://doi.org/10.3847/0004-637x/823/2/102)
- Choquet, É., Pueyo, L., Hagan, J. B., et al. 2014, *Space Telescopes and Instrumentation 2014: Optical, Infrared, and Millimeter Wave*, 9143, 914357, doi: [10.1117/12.2056672](https://doi.org/10.1117/12.2056672)
- Correia, S., Duchêne, G., Reipurth, B., et al. 2013, *Astronomy and Astrophysics*, 557, 1, doi: [10.1051/0004-6361/201220681](https://doi.org/10.1051/0004-6361/201220681)
- Da Rio, N., Robberto, M., Hillenbrand, L. A., Henning, T., & Stassun, K. G. 2012, *Astrophysical Journal*, 748, doi: [10.1088/0004-637X/748/1/14](https://doi.org/10.1088/0004-637X/748/1/14)
- De Furio, M., Reiter, M., Meyer, M. R., et al. 2019, *ApJ*, 886, 95, doi: [10.3847/1538-4357/ab4ae3](https://doi.org/10.3847/1538-4357/ab4ae3)
- Dotter, A. 2016, *The Astrophysical Journal Supplement Series*, 222, 8, doi: [10.3847/0067-0049/222/1/8](https://doi.org/10.3847/0067-0049/222/1/8)
- Duchêne, G., & Kraus, A. 2013, 1, doi: [10.1146/annurev-astro-081710-102602](https://doi.org/10.1146/annurev-astro-081710-102602)
- Duchêne, G., Lacour, S., Moraux, E., Goodwin, S., & Bouvier, J. 2018, *Monthly Notices of the Royal Astronomical Society*, 478, 1825, doi: [10.1093/mnras/sty1180](https://doi.org/10.1093/mnras/sty1180)
- Duchene, G., Lacour, S., Moraux, E., et al. 2018, *Monthly Notices of the Royal Astronomical Society*, 1836, 1825, doi: [10.1093/mnras/sty1180](https://doi.org/10.1093/mnras/sty1180)
- Duquennoy, A., & Mayor, M. 1991, *A&A*, 500, 337
- Gennaro, M., Prada Moroni, P. G., & Tognelli, E. 2012, *Monthly Notices of the Royal Astronomical Society*, 420, 986, doi: [10.1111/j.1365-2966.2011.19945.x](https://doi.org/10.1111/j.1365-2966.2011.19945.x)
- Gladwin, P. P., Kitsionas, S., Boffin, H. M., & Whitworth, A. P. 1999, *Monthly Notices of the Royal Astronomical Society*, 302, 305, doi: [10.1046/j.1365-8711.1999.02136.x](https://doi.org/10.1046/j.1365-8711.1999.02136.x)
- Hunter, J. D. 2007, *Computing in Science & Engineering*, 9, 90, doi: [10.1109/MCSE.2007.55](https://doi.org/10.1109/MCSE.2007.55)
- Jerabkova, T., Beccari, G., Boffin, H. M. J., et al. 2019, *A&A*, 627, A57, doi: [10.1051/0004-6361/201935016](https://doi.org/10.1051/0004-6361/201935016)
- Kirkpatrick, J. D., Gelino, C. R., Cushing, M. C., et al. 2012, *ApJ*, 753, 156, doi: [10.1088/0004-637X/753/2/156](https://doi.org/10.1088/0004-637X/753/2/156)
- Köhler, R., Petr-Gotzens, M. G., McCaughrean, M. J., et al. 2006, *Proceedings of the International Astronomical Union*, 2, 114, doi: [10.1017/S1743921307003912](https://doi.org/10.1017/S1743921307003912)
- Kraus, A. L., Ireland, M. J., Martinache, F., & Hillenbrand, L. A. 2011, *Astrophysical Journal*, 731, doi: [10.1088/0004-637X/731/1/8](https://doi.org/10.1088/0004-637X/731/1/8)
- Kroupa, P. 2001, *MNRAS*, 322, 231, doi: [10.1046/j.1365-8711.2001.04022.x](https://doi.org/10.1046/j.1365-8711.2001.04022.x)
- Kuhn, M. A., Hillenbrand, L. A., Sills, A., Feigelson, E. D., & Getman, K. V. 2019, *The Astrophysical Journal*, 870, 32, doi: [10.3847/1538-4357/aaf8c](https://doi.org/10.3847/1538-4357/aaf8c)
- Larson, R. B. 1995, *Monthly Notices of the Royal Astronomical Society*, 272, 213, doi: [10.1093/mnras/272.1.213](https://doi.org/10.1093/mnras/272.1.213)
- Marois, C., Correia, C., Galicher, R., et al. 2014, *Adaptive Optics Systems IV*, 9148, 91480U, doi: [10.1117/12.2055245](https://doi.org/10.1117/12.2055245)
- Mawet, D., Milli, J., Wahhaj, Z., et al. 2014, *Astrophysical Journal*, 792, doi: [10.1088/0004-637X/792/2/97](https://doi.org/10.1088/0004-637X/792/2/97)
- McKinney, W., et al. 2010, in *Proceedings of the 9th Python in Science Conference*, Vol. 445, Austin, TX, 51–56
- Petr, M. G., Coude du Foresto, V., Beckwith, S. V. W., Richichi, A., & McCaughrean, M. J. 1998, *The Astrophysical Journal*, 500, 825, doi: [10.1086/305751](https://doi.org/10.1086/305751)
- Price-Whelan, A. M., Sipőcz, B. M., Günther, H. M., et al. 2018, *AJ*, 156, 123, doi: [10.3847/1538-3881/aabc4f](https://doi.org/10.3847/1538-3881/aabc4f)
- Pueyo, L. 2016, doi: [10.3847/0004-637X/824/2/117](https://doi.org/10.3847/0004-637X/824/2/117)
- Reipurth, B., Guimarães, M. M., Connelley, M. S., & Bally, J. 2007, *The Astronomical Journal*, 134, 2272, doi: [10.1086/523596](https://doi.org/10.1086/523596)
- Robberto, M., Soderblom, D. R., Bergeron, E., et al. 2013, *Astrophysical Journal, Supplement Series*, 207, doi: [10.1088/0067-0049/207/1/10](https://doi.org/10.1088/0067-0049/207/1/10)
- Scally, A., Clarke, C., & McCaughrean, M. J. 1999, *Monthly Notices of the Royal Astronomical Society*, 306, 253, doi: [10.1046/j.1365-8711.1999.02513.x](https://doi.org/10.1046/j.1365-8711.1999.02513.x)
- Scott, D. W. 1979, *Biometrika*, 66, 605
- Slesnick, C. L., Hillenbrand, L. A., & Carpenter, J. M. 2004, *ApJ*, 610, 1045, doi: [10.1086/421898](https://doi.org/10.1086/421898)

- Soummer, R., Pueyo, L., & Larkin, J. 2012, *Astrophysical Journal Letters*, 755, 1,
doi: [10.1088/2041-8205/755/2/L28](https://doi.org/10.1088/2041-8205/755/2/L28)
- Spiegel, D. S., Burrows, A., & Milsom, J. A. 2011,
Astrophysical Journal, 727, 1,
doi: [10.1088/0004-637X/727/1/57](https://doi.org/10.1088/0004-637X/727/1/57)
- Spurzem, R., Giersz, M., Heggie, D. C., & Lin, D. N. 2009,
Astrophysical Journal, 697, 458,
doi: [10.1088/0004-637X/697/1/458](https://doi.org/10.1088/0004-637X/697/1/458)
- Stassun, K. G., Feiden, G. A., & Torres, G. 2014, *New Astronomy Reviews*, 60-61, 1,
doi: [10.1016/j.newar.2014.06.001](https://doi.org/10.1016/j.newar.2014.06.001)
- van der Walt, S., Colbert, S. C., & Varoquaux, G. 2011,
Computing in Science Engineering, 13, 22
- Virtanen, P., Gommers, R., Oliphant, T. E., et al. 2020,
Nature Methods, 17, 261,
doi: <https://doi.org/10.1038/s41592-019-0686-2>
- Wang, J. J., Ruffio, J.-B., De Rosa, R. J., et al. 2015,
pyKLIP: PSF Subtraction for Exoplanets and Disks.
<http://ascl.net/1506.001>
- Winters, J. G., Henry, T. J., Jao, W.-C., et al. 2019, *The Astronomical Journal*, 157, 216,
doi: [10.3847/1538-3881/ab05dc](https://doi.org/10.3847/1538-3881/ab05dc)